Characterizing fractional quantum Hall states in lattice models

Master's Thesis

Madhav Mohan

Condensed Matter Theory group
Department of Physics
University of Zürich

Supervisors:
Prof. Titus Neupert
Dr. Bartholomew Andrews

March 1, 2021

Preface

We provide an introduction in Chapter 1, and discuss the theoretical concepts that inform our research in Chapter 2. The computational methods involved in our research are discussed in Chapter 3. The research, including an analysis and discussion of our results forms Chapter 4.
Chapter 4, as well as parts of Section 2.4 consists of content from the original paper:
"Abelian topological order of $\nu = 2/5$ and $3/7$ fractional quantum Hall states in lattice models", B. Andrews, M. Mohan and T. Neupert, Phys. Rev. B **103**, 075132 (2021) [1]. My contribution to this project involved the majority of the data collection (this included running the iDMRG computations for the FCI lattice systems and obtaining the area law plots).
I was also responsible for a large part of the data analysis, and contributed to the development of the systematic routine that we developed towards the aim of computing the topological entanglement entropy accurately.
Calculations were performed using the TeNPy Library (version 0.5.0) [2] and GNU PARALLEL [3].

Acknowledgements

Firstly, I want to thank Prof. Titus Neupert for his guidance and support throughout the research period, and for allowing me the valuable opportunity to conduct research in his group. I thank him also for valuable discussions that helped to direct the course of the research—this thesis would not have been possible without his help. I had a strongly positive experience during my time in the group, and this played a major role in my decision to pursue my scientific career further.

I would like to thank Dr. Bartholomew Andrews, my supervisor for this thesis, for the several illuminating discussions and constructive suggestions. I have learned so much from our interactions that will guide me in my scientific career. His scientific rigor, extensive knowledge of the subject along with his empathy and patience make him an ideal supervisor, and I thoroughly enjoyed working with him.

Further, I thank my colleagues Pascal Vecsei, Anar Bold, Manuel Sommerhalder and Daniel Hernandez. They have been encouraging and supportive in many ways to do with both physics and life, and have ensured that I will look back fondly on my time in Zürich.

Finally, I express my gratitude for my parents who continue to inspire me, and motivate me to keep striving and improving.

Abstract

The theoretical investigation of the fractional quantum Hall effect (FQHE) has been a reliable source of exciting physics since its discovery in 1982. It exhibits unusual phenomena such as fractional statistics and fractional charge, and has illuminated the connection between topology and physics.
The FQHE has been generalized on lattices—notably, these systems (termed fractional Chern insulators) have been shown to exhibit lattice-specific FQH states. FCIs have been proposed as candidate systems for topological quantum computing, which further motivates the investigation of their ground state statistics and stability.
In this thesis, we study FQH states on a lattice. We work in the MPS framework, and use the iDMRG algorithm on an infinite cylinder to probe the topological order of the $\nu = 2/5$ and $3/7$ ground states for the Hofstadter model. We introduce an efficient algorithm for this purpose, and demonstrate Abelian order for nearest-neighbor interactions by computing the topological entanglement entropy. We discuss the sensitivity of this method with respect to interaction range and strength.
The Hofstadter model also exhibits FCIs with Chern numbers $|C| > 1$. We investigate the stability of these states and aim to characterize their breakdown transitions. We use iDMRG to compute the entanglement energy spectrum and correlation length with respect to interaction strength, in order to determine the central charge and resulting phases.

Contents

Chapter 1

Introduction

Understanding the physical properties of quantum many-body systems is a problem of central importance in theoretical physics. The challenges involved have necessitated the development of new physics, notably new methods of classifying phases of matter through topological order, for which the 2016 Nobel prize was awarded to Thouless, Haldane and Kosterlitz [4]—and thus, in the last few decades, the field has risen to prominence.

This new landscape of condensed matter research was sparked by the remarkable discoveries of the integer quantum Hall effect (IQHE) and the fractional quantum Hall effect (FQHE) in 1980 and 1982 respectively [5, 6]. The experimental setup involves a two-dimensional electron gas in a strong perpendicular magnetic field, at low temperatures.
On driving a current through the sample, one observes that the transverse electrical conductivity (termed the *Hall conductivity*) σ_{xy} plateaus in steps and is quantised, that is, $\sigma_{xy} = e^2\nu/(h)$ where ν takes integer values. The key to this unusual behavior was identified to be the disorder in the system. Later on, quantised plateaus in the Hall conductivity were observed at fractional values of e^2/h, with the most prominent fractions being $\nu = 1/3$ and $2/5$.

Following these discoveries, several theories have been proposed and experiments conducted to unravel these truly remarkable phenomena. The physics of the IQHE is now well understood, and the explanation involves the quantum mechanics of non-interacting electrons. Crucially, the Hall conductivity was understood as a topological invariant of the system, which explained the robustness of the IQHE and illuminated the connection between topology and quantum mechanics [7].
The study of the FQHE on the other hand presents a significant hurdle—the system involves energy bands (that arise for charged particles in a magnetic field and are termed *Landau levels*) that are fractionally-filled, and this leads to a highly degenerate ground state. The effect is stabilized by electron-electron interactions that would lift the degeneracy—however, the corresponding perturbation theory involves a macroscopically large Hamiltonian that is difficult to diagonalize.

Despite this challenge, there has been significant theoretical progress, with creative approaches involving educated guesses for the ground state wavefunctions [8] and analogies between the IQHE and FQHE [9]. The FQHE can be generalized on

the lattice through *fractional Chern insulators* (FCIs), which in the Landau-level limit (for our purpose, this denotes flat Chern bands with unit Chern number) share the universal topological properties of the FQHE [10]. Away from this limit FCIs provide new physics that is not present in the continuum— as the physics of FCIs for higher Chern numbers cannot be continuously connected to the continuum physics [11, 12]. FCIs also provide a way to stabilize FQHE states without the need for a strong magnetic field [10], and thus their study is of interest for technologies, notably topological quantum computing—that proposes fault-tolerant quantum computation by braiding the anyonic excitations of the ground state [13]. We discuss the main theoretical concepts introduced above that inform our research in Chapter 2, notably the concept of fractional statistics and topological order, and further discuss the models that stabilize these states on lattices.

Numerical methods present an attractive option for the investigation of quantum many-body systems, given that analytic solutions often do not exist. Matrix product state (MPS) based methods are well established tools for this simulation—in particular, we used the infinite Density Matrix Renormalization Group (iDMRG) algorithm on an infinite cylinder for the computation of the ground state wavefunction of FCIs. In Section 3, we introduce and motivate this method, why it is suitable for our purposes, and its limitations. We also talk about various numerical techniques that we can use to characterize these FQH states, and to confirm their topological nature.
In Section 4, we detail the computational investigation of excitations of the FQH ground state, and discuss the current status of the field. We investigate the topological order of $\nu = 2/5$ and $3/7$ FQH states in lattice models, and present and discuss our results. In one of the central results of this thesis, we show that these FQH states exhibit Abelian topological order in the case of nearest-neighbor interactions. Also important is the algorithm that we devise for this purpose, that allows us to compute the topological entanglement entropy accurately, and will be of interest for further studies that aim to characterize topological order in FQH states.

Various numerical studies have stabilized FCIs away from the Landau-level limit [14–18]. Thus, it is of interest to investigate the stability of the FCI states, which we study for systems with higher Chern number bands. We describe this research in Chapter 5.

Chapter 2

Theory

The theory of quantum many-body systems, notably topological insulators and the fractional quantum Hall effect (FQHE) presents one of the biggest challenges in modern physics research. There has been a lot of progress made on the theoretical aspects of FQHE—theorists have come up with ground state wavefunctions that explain the physics at various filling factors, and have described the anyonic excitations that these ground states support. Further, physicists have proposed uses for these exotic fractional quantum Hall (FQH) fluids, notably the use of these anyonic excitations to realize topological quantum computing [13]. As we shall see, there are certain factors that make the theoretical study of the FQHE challenging, and this has led to some creative approaches, and further, has shed light on the celebrated role of topology in physics.
In this chapter, we introduce and explain important theoretical concepts that one needs to be familiar with, in order to investigate quantum many-body systems—and in our case, FQH states on lattices.
Section 2.1 considers the physics of particles in a magnetic field, section 2.2 introduces the physics of the FQHE along with the fundamental concepts of fractional statistics and topological order. In section 2.3 we consider the generalizations of the FQHE to two-dimensional lattices in the form of *fractional Chern insulators*, and highlight the criteria a model should have to support such fractional states. Finally, in section 2.4, we look at the *Hofstadter model*, and discuss how we select configurations that stabilize the FQHE and contain other features of interest, such as Chern bands with $|C| > 1$.

2.1. Energy levels in a magnetic field

We present a brief recap of the physics of particles in a magnetic field—in particular, we introduce the concepts that will aid us in the discussion of the FQHE.
We can set up the problem by writing the quantum Hamiltonian that describes an electron confined to a two-dimensional (we consider xy) plane, along with a perpendicular magnetic field $\mathbf{B} = \nabla \times \mathbf{A}$ where $\mathbf{A}$ is the gauge potential. This is

given by

$$H = \frac{1}{2m_e}(\mathbf{p} + e\mathbf{A})^2 \tag{2.1}$$

where $\mathbf{p}$ is the canonical momentum, and e and m_e are the charge and mass of the electron respectively.
Choosing the *Landau gauge*, $\mathbf{A} = xB\hat{y}$ and introducing an ansatz for the wavefunction based on translational invariance in the y direction allows us to interpret the Hamiltonian as that of a harmonic oscillator in the x direction

$$H_k = \frac{1}{2m_e}p_x^2 + \frac{m\omega_B^2}{2}(x + kl_B^2)^2 \tag{2.2}$$

with frequency as the cyclotron frequency $\omega_B = eB/m$, and the *magnetic length* $l_B = \sqrt{\hbar/(eB)}$, which is the characteristic length scale for quantum phenomena in the presence of a magnetic field. The energy eigenvalues also then correspond to those of a harmonic oscillator

$$E_n = \hbar\omega_B\left(n + \frac{1}{2}\right) \tag{2.3}$$

We have obtained equally spaced energy levels of a particle in the presence of a magnetic field, such that the gap between levels is proportional to the magnetic field applied. We call these *Landau levels*. It is also straightforward to see that these levels are degenerate if we write the wavefunction explicitly

$$\psi_{n,k}(x,y) \propto \exp[iky]H_n(x + kl_B^2)\exp\left[-\frac{1}{2l_B^2}(x + kl_B^2)^2\right] \tag{2.4}$$

where H_n is the n^{th} Hermite polynomial.

We now choose the symmetric gauge, $\mathbf{A} = \frac{1}{2}(-By\hat{x} + Bx\hat{y})$. This gauge preserves the rotational symmetry about the origin, allowing us to define the angular momentum—a good quantum number for our gauge choice. We note also that the gauge breaks the translational symmetries in x- and y-direction. We tackle this problem with an algebraic approach.

We define the following momentum operators

$$\pi = \mathbf{p} + e\mathbf{A} \rightarrow a = \frac{1}{2e\hbar B}(\pi_x - i\pi_y) \tag{2.5}$$

$$\tilde{\pi} = \mathbf{p} - e\mathbf{A} \rightarrow b = \frac{1}{2e\hbar B}(\pi_x + i\pi_y) \tag{2.6}$$

and the ladder operators allow us to construct the eigenstates as

$$|n, m\rangle \propto a^{\dagger n} b^{\dagger m} |0, 0\rangle \tag{2.7}$$

where n and m track the Landau level and the degeneracy respectively. Important also is the *lowest Landau level* (LLL), for which we must have

$$a |0, m\rangle = 0 \tag{2.8}$$

Let $z = x - iy$ and the corresponding derivative $\partial = (\partial_x + i\partial_y)/2$. This allows us to write the ladder operators as

$$a = -i\sqrt{2}\left(l_B \bar{\partial} + \frac{z}{4l_B}\right) \tag{2.9}$$

$$b = -i\sqrt{2}\left(l_B \partial + \frac{\bar{z}}{4l_B}\right) \tag{2.10}$$

This allows us to write 2.8 as a differential equation, the solution for which is given as

$$\psi_{LLL,m}(z) = f(z) e^{-|z|^2/4l_B^2} \tag{2.11}$$

for any holomorphic function $f(z)$. The lowest LLL state must be annihilated by a and b, and this implies that this state $\psi_{LLL,m=0} \propto e^{-|z|^2/4l_B^2}$. Further we construct the higher LLL states by acting with $b^\dagger$ on $\psi_{LLL,m=0}$, and thus

$$\psi_{LLL,m}(z) \propto \left(\frac{z}{l_B}\right)^m e^{-|z|^2/4l_B^2} \tag{2.12}$$

One can also construct the higher LL wavefunctions—one acts with $a^\dagger$ on the LLL states. Defining the angular momentum operator $J = i\hbar(x\partial_y - y\partial_x)$, we see that the states are eigenfunctions of J, in particular for the LLL states we have

$$J\psi_{LLL,m} = \hbar m \psi_{LLL,m} \tag{2.13}$$

We refer the reader to [19, 20] and [21], for a more pedagogical and thorough introduction of QHE physics, along with the associated derivations.

In our discussion, we neglect the spin degree of freedom of the electron—in the presence of a large magnetic field B, the energies of spins-↑ and ↓ are split by $\Delta = 2\mu_B B$ (this is the Zeeman effect), where μ_B is the Bohr magneton. Thus large energies will be needed to flip the spins, and if we restrict our study to low temperatures the electrons can be considered spinless.

2.2. Fractional Quantum Hall Effect

The physics of the FQHE is dominated by the electron-electron interactions, which is negligible in the theoretical discussion of the IQHE [9]. Such interactions can be modelled, for example, with the Coulomb potential. To make these interactions dominant in the physics, one imposes the following requirement: $\hbar\omega_B \gg V_{Coulomb} \gg V_{disorder}$, where ω_B is the cyclotron frequency associated with the energies of our Landau level, as in Eq. 2.3. To fulfil this requirement, we must conduct a Hall experiment at even lower temperatures and stronger magnetic fields than in the IQHE, and further, we require a pure sample.

While the IQHE ground state is unique, a partially filled Landau level ($\nu < 1$) presents ${}^{N}C_{\nu N}$ possible configurations (N being the number of states in the level) which leads to highly degenerate ground states that cannot be dealt with the use of perturbation theory. This presents a major challenge from an analytic point of view, and has led to various creative theoretical approaches, one of which we now introduce.

2.2.1. Laughlin states

Laughlin sought to capture the physics at the filling fractions $\nu = 1/m$, where m is an odd integer, by giving an ansatz for the ground state wavefunction. The guess was motivated by angular momentum arguments [19]—for such discussions, we often choose the symmetric gauge. Recall that the one-particle LLL wavefunction is given by 2.12.

We can motivate the general form of the many-body LLL wavefunction (one approach, given by solving a two-body problem for interacting electrons in the LLL, is provided in [21]), which is given as

$$\psi_{LLL}(z_1, ..., z_N) = \tilde{\psi}(z_1, ..., z_N) e^{-\sum_{i=1}^{N} |z_i|^2/4l_B^2} \tag{2.14}$$

for an analytic function $\tilde{\psi}$, that is asymmetric under particle exchange (thus ensuring Pauli's exclusion principle). Laughlin's ground state wavefunction ansatz is

$$\tilde{\psi}(z_1, \ldots, z_N) = \prod_{i<j} (z_i - z_j)^m \tag{2.15}$$

We notice that $\tilde{\psi}$ vanishes (with a zero of order m) when two electrons come close, and the exponential term from Eq. 2.14 drops rapidly if electrons are far apart from the origin. The wavefunction is thus peaked at a certain radius, such that the two competing effects are balanced.

We conduct some checks on this function—firstly, we note that this function is indeed asymmetric, when m is an odd integer. By examining the eigenvalues of

the angular momentum, we can show that m is the relative angular momentum of the electrons [21]. Further, considering the first particle z_1, we find $m(N-1)$ powers of z_1 in $\tilde{\psi}$, which gives the maximum angular momentum of the first particle as $m(N-1)$ and the corresponding radius $R \approx \sqrt{2mN}l_B$ (such that the droplet area $A = \pi R^2$). The number of states in the Landau level is then given by

$$N_\phi = \frac{\Phi}{\Phi_0} = \frac{A}{2\pi l_B^2} = m(N-1) \tag{2.16}$$

which confirms the expected filling fraction as

$$\nu = \frac{N}{N_\phi} = \frac{N}{m(N-1)} \approx \frac{1}{m} \tag{2.17}$$

where the approximation holds for large N. For a small number of particles, the Laughlin wavefunction has large overlap (often greater than 99%) with the true ground state (obtained by considering the full Hamiltonian, with electron-electron interactions characterized by a Coulomb potential)—although this overlap is likely to be negligible for a macroscopic number of particles [21]. The main attraction of this state is that it lies in the same *universality class* as the true ground state—this ensures that the states have the same topological properties, such as the fractional statistics [22].

2.2.2. Excitations of the Laughlin ground state

Having introduced the Laughlin ground state, we now move on to the excitations this state supports—in particular we consider the *quasi-hole* . Importantly, we also introduce the concept of fractional statistics that we later investigate in our research.

Quasi-Holes

The many-body wavefunction describing a quasi-hole at position $z_{\mathbf{hole}} \in \mathbb{C}$ must fulfil the criterion that the probability density (the probability of finding an electron) vanishes at z_{hole}. This motivates the following form

$$\widetilde{\psi}_{\text{hole}}(z_{\text{hole},z_1,\ldots,z_N}) = \prod_{i=1}^{N}(z_i - z_{\text{hole}}) \prod_{k<l}(z_k - z_l)^m \tag{2.18}$$

We can consider the case of M quasi-holes in our fluid with positions $z_{\text{hole},a}$ (for $a = 1, \ldots, M$) by generalising Eq. 2.18 as

$$\widetilde{\psi}_{\text{hole}}(z_{\text{hole}}, z_1, \ldots, z_N) = \prod_{a=1}^{M} \prod_{i=1}^{N} (z_i - z_{\text{hole},a}) \prod_{k<l} (z_k - z_l)^m \tag{2.19}$$

This now sets the stage for introducing a remarkable characteristic of the FQHE—that of fractional charge.

We will derive this fractional charge (along with the corresponding statistics) later on—for now we present a simple argument to motivate the concept. We fix m quasi-holes at the same location z_{hole} and write the corresponding wavefunction

$$\widetilde{\psi}_{\text{M-hole}}(z_{\text{hole}}, z_1, \ldots, z_N) = \prod_{i=1}^{N} (z_i - z_{\text{hole}})^m \prod_{k<l} (z_k - z_l)^m \tag{2.20}$$

By comparing this to the ground state wavefunction in Eq. 2.15, we notice that $\widetilde{\psi}_{\text{M-hole}}$ describes the absence of one electron at z_{hole}. Hence, m holes correspond to the deficit of one electron, and one hole must carry the charge $+e/m$ that corresponds to $1/m^{th}$ of this absence.

We make some more statements about the fractional charge, as it is a truly unusual phenomenon. Firstly, we note that the total charge of the system will always be an integer multiple of e (thus ensuring no physical laws are violated). However, in the liquid, the fractional charged excitations act as independent particles. These excitations have also been experimentally observed in shot noise experiments [23]. Notably, there is strong recent experimental evidence for anyons—their fractional statistics have been directly observed using a Fabry-Perot interferometer [24], and inferred from current correlations in an approach that collides anyons in a two-dimensional electron gas (2DEG)[25].

We now discuss the quantum statistics of these excitations as this concept is intimately connected to our research. We emphasize that there are certain steps and substitutions in the derivation that we do not discuss here—our main purpose in this section is to provide the motivation behind the form of the Berry connection, which is a crucial ingredient in the discussion of the statistics. We refer the reader to [26] for a more involved derivation.

We consider a state with M quasi-holes, $|\psi\rangle = Z^{-1/2} |\eta_1, \ldots, \eta_M\rangle$, where $Z = \langle \eta_1, \ldots, \eta_M | \eta_1, \ldots, \eta_M \rangle$ gives the normalization.

We must compute the holomorphic Berry connection,

$$\mathcal{A}_\eta(\eta, \bar{\eta}) = -i \langle \psi | \frac{\partial}{\partial \eta} |\psi\rangle = -\frac{i}{2} \frac{\partial \log Z}{\partial \eta} \tag{2.21}$$

where we have used the fact that $|\eta\rangle$ is holomorphic and thus $\frac{\partial Z}{\partial \eta} = \langle \eta | \frac{\partial}{\partial \eta} | \eta \rangle$. Similarly one computes the anti-holomorphic connection $\mathcal{A}_{\bar{\eta}}$. To simplify the calculation for Z (that would otherwise require computing a macroscopic number of integrals), we employ a plasma analogy for the ground state wavefunction that simplifies the computation of expectation values—in our case, the normalization—by considering an analogous (classical) statistical mechanical system of a plasma of particles with charge $-m$, moving in two dimensions. Concretely, one can write a classical Boltzmann distribution function with associated potential $U(z_i)$ that is analogous to the Laughlin probability density (computed using Eq. 2.15),

$$e^{-\beta U(z_i)} = \prod_{i<j} \frac{|z_i - z_j|^{2m}}{l_B^{2m}} e^{-\sum_i |z_i|^2 / 2l_B^2} \tag{2.22}$$

In the plasma, then, the quasi-hole is interpreted as a positively charged impurity that *screens* the negative charges—this modifies the electric potential of the impurity such that it falls off exponentially. Using Eq. 2.22 and modifying the potential to account for the impurities, one obtains the classical potential (for M impurities) as

$$\begin{aligned} U(z_k, \eta_i) = &- m^2 \sum_{k<l} \log\left(\frac{|z_k - z_l|}{l_B}\right) - m \sum_{k,i} \log\left(\frac{|z_i - \eta_i|}{l_B}\right) - \sum_{i<j} \log\left(\frac{|\eta_i - \eta_j|}{l_B}\right) \\ &+ \frac{m}{4l_B^2} \sum_{k=1}^{N} |z_k|^2 + \frac{1}{4l_B^2} \sum_{i=1}^{M} |\eta_i|^2 \end{aligned}$$

In the regime where the distance between any two impurities $|\eta_i - \eta_j|$ is greater than the Debye length λ (the characteristic length scale in screening), one can carry out analytical simplifications and obtain the normalization as

$$Z = C \exp\left(\frac{1}{m} \sum_{i<j} \log|\eta_i - \eta_j|^2 - \frac{1}{2ml_B^2} \sum_i |\eta_i|^2\right) \tag{2.23}$$

which allows us to compute the Berry connections over the configuration space of M quasi-holes from Eq. 2.21 :

$$\mathcal{A}_{\eta_i} = -\frac{i}{2m} \sum_{j \neq i} \frac{1}{\eta_i - \eta_j} + \frac{i\bar{\eta}_i}{4ml_B^2} \tag{2.24}$$

$$\mathcal{A}_{\bar{\eta}_i} = +\frac{i}{2m} \sum_{j \neq i} \frac{1}{\bar{\eta}_i - \bar{\eta}_j} - \frac{i\eta_i}{4ml_B^2} \tag{2.25}$$

Fractional charge and statistics

The derivation of the fractional charge follows from Eqs. 2.24 and 2.25. We move one of the quasi-holes on a closed path C. If we move on a path that does not enclose any anyons, the first term in the connection vanishes and we get

$$\mathcal{A}_\eta = \frac{i\bar{\eta}}{4ml_B^2}, \mathcal{A}_{\bar{\eta}} = -\frac{i\eta}{4ml_B^2} \tag{2.26}$$

The quasi-hole picks up a phase shift given by the *Berry phase*

$$e^{i\gamma} = \exp\left(-i \oint_C \mathcal{A}_\eta d\eta + \mathcal{A}_{\bar{\eta}} d\bar{\eta}\right) \tag{2.27}$$

from which we obtain

$$\gamma = \frac{e\phi}{m\hbar} \tag{2.28}$$

where ϕ gives the magnetic flux that the path encloses. One recognizes that this must be equal to the Aharonov-Bohm phase of the particle. We recall that this phase associated with a particle of charge q is $\gamma = q\phi/\hbar$, which allows us to read off the hole charge as $q = e/m$.
Now, consider again the motion of a quasi-hole η_a in a closed path C, however unlike in the previous argument, let this path enclose quasi-hole η_b. As with the fractional charge, the second term of Eqs. 2.24 and 2.25 gives the Aharanov-Bohm phase. The first term gives the statistics

$$e^{i\gamma} = \exp\left(-\frac{1}{2m} \oint_C \frac{d\eta_a}{\eta_a - \eta_b} + \text{h.c.}\right) = e^{2\pi i/m} \tag{2.29}$$

where we evaluated the integral using the residue theorem. We have derived the phase from η_a moving around η_b. One can consider one rotation (captured in Eq. 2.29) as corresponding to two particle exchanges, hence the phase picked up in one exchange is $e^{\pi i/m}$. In three dimensions, we recall the exchange statistics are completely given by the phase $e^{i\pi\alpha}$ in the equation $\psi(\mathbf{r}_1, \mathbf{r}_2) = e^{i\pi\alpha}\psi(\mathbf{r}_2, \mathbf{r}_1)$ such that $\alpha = 0$ describes bosons and $\alpha = 1$ describes fermions. Thus the derived statistics correspond to $\alpha = 1/m$. This is again rather unusual —as we have seen, two exchanges do not bring the wavefunction back to the original state (unlike in the case of fermions and bosons)— and has its root in the fact that we restrict our particles to move in two dimensions. One also has to consider the topology of the worldlines traced by particles in spacetime, which is fundamentally different in two dimensions. A detailed discussion on anyons and the role of dimensions in

topology can be found in [27]. We discuss the anyonic statistics further in Chapter 4, and compute them for FQH states at certain filling factors of interest.

2.2.3. Topological order

The FQHE statistics yield the concept of topological order. Let us consider the problem of characterizing these states—to this end, we note that we cannot distinguish QH states through local order parameters or symmetries.
In [28], it is proposed that QH phases are an entirely new type of matter with *topological order*, characterized notably by their ground state degeneracy. We discuss this concept further in Chapter 4, and investigate the order for certain filling fractions of interest.

To summarize, in this section we have introduced the physics of the FHQE—we looked at the main challenge in investigating these states that has its roots in the highly degenerate ground state. We motivated the Laughlin wavefunction ansatz that captures the physics of the FQHE at filling fractions $\nu = 1/m$ (for m an odd integer) as it lies in the same universality class as the true ground state. We discussed the excitations of the Laughlin ground state, and introduced important concepts characteristic to the FQHE such as fractional charge, statistics and topological order.

2.3. Fractional Chern Insulators

In our research, we investigated FQH states on a lattice, which we introduce and motivate here. We recall that Chern insulators are band insulators with the single-particle spectrum characterized by a finite Chern number, such that the filled bands (termed *Chern bands*) can still have a finite, quantized Hall conductivity—this has its roots in the breaking of time-reversal symmetry [29]. In the models we will consider, one breaks the TR symmetry by including complex hopping phases in the model Hamiltonian.

If instead, a Landau level—arising from a lattice Hamiltonian— is fractionally filled, the interaction term (in the many-body Hamiltonian) is turned on, and the resulting system exhibits a quantised fractional Hall conductance, we term it a *fractional Chern insulator*.
Concretely, we look at two-dimensional systems with interacting particles, that have a topologically ordered many-body ground state possessing topological properties (such as the anyonic excitations, and a quantized Hall conductivity) that, in the Landau-level limit, match with those of the FQHE at the corresponding filling factor ν [22].

There exist a number of tight-binding models that can host these fractional states. Let us consider the desirable criteria these models must possess. Firstly, in order to resemble Landau levels, the Chern bands in the model must have a flat energy dispersion and a flat Berry curvature [30]. A flat energy dispersion ensures that the inter-particle interactions dominate the physics. Further, it is desirable to have a large band gap such that higher bands do not contribute to the physics. The requirement is formulated as $W \ll V_{int} \ll E_G$, where W is the bandwidth, V_{int} is the interaction strength and E_G the band gap. This requirement can be quantified by the *gap-to-width ratio* $F = E_G/W$, which should be large.

However, these criteria are not strict: for instance, we note that FCI states have been shown to survive even when the interaction strength is greater than the bandgap [17].

The FCIs go one step further than simply recovering FQH physics. One recalls the Landau-level limit for FQHE, which for our purposes denotes the requirement of flat bands and unit Chern number. However, FQH states have been shown to persist even when these conditions are violated. In particular, [17] and [31] show that FCIs survive even if the Chern band we consider is not flat or isolated from other bands. Further, FCI states have also been observed in Chern bands with higher Chern numbers, $|C| > 1$ [14]—this is a significant result as the physics of FCIs at higher $|C|$ cannot be continuously connected to the Landau level physics of the continuum [11, 12]. Thus, these FQH states are specific to the lattice, and allow us to state that FCIs generalize the FQHE states in continuum Landau levels to lattices. These states are found at the filling factor [14]

$$\nu = \frac{r}{kr|C| - \mathrm{sgn}(C)} \tag{2.30}$$

where r is an integer, $k = 1, 2$ for bosons and fermions respectively.

2.4. Hofstadter model

2.4.1. Single-particle Hamiltonian

We consider spinless fermions hopping on a square lattice in the xy-plane subject to a perpendicular magnetic field. A charged particle moving in a magnetic field picks up a phase, referred to as the Aharanov-Bohm phase [32], and the corresponding phase on a lattice is called the *Peierls phase*. The precise value of the phase θ_{ij} along a particular path is dependent on the gauge, since $\theta_{ij} = \int_i^j \mathbf{A} \cdot d\mathbf{l}$, where $\mathbf{A}$ is the vector potential and $d\mathbf{l}$ is the infinitesimal line element from sites i to j [33]. In our research, we work with the x-direction Landau gauge such that $\mathbf{A} = Bx\hat{y}$.

For this choice of gauge, the fermions only acquire a phase when they hop in the x-direction. The Hofstadter model [34] describes the single-particle Hamiltonian that sets up the Chern bands, and is given as

$$H_0 = \sum_{\langle ij \rangle_1} \left[t e^{(i\theta_{ij})} a_i^\dagger a_j + H.c. \right] \tag{2.31}$$

where t is the hopping amplitude, $a^\dagger(a)$ are the creation (annihilation) operators for spinless fermions, and $\langle ij \rangle_{\kappa'}$ denotes pairs of κ'th nearest-neighbor sites on the square lattice.

Crucially, there are two competing area scales in the model, the irreducible area of a flux quantum and the magnetic unit cell area (we discuss the latter in section 2.4.2). This frustration is typically quantified using the flux density, defined as $n_\phi = BA_{\mathrm{UC}}/\phi_0 = p/q$, where $\phi_0 = h/e$ is the flux quantum and p, q are coprime integers.

Finally, we note that since the kinetic energy of the system is quenched for the FQH states, the interaction Hamiltonian dominates the physics. Ideally, the role of the single-particle Hamiltonian is simply to facilitate tuning to the correct system configurations.

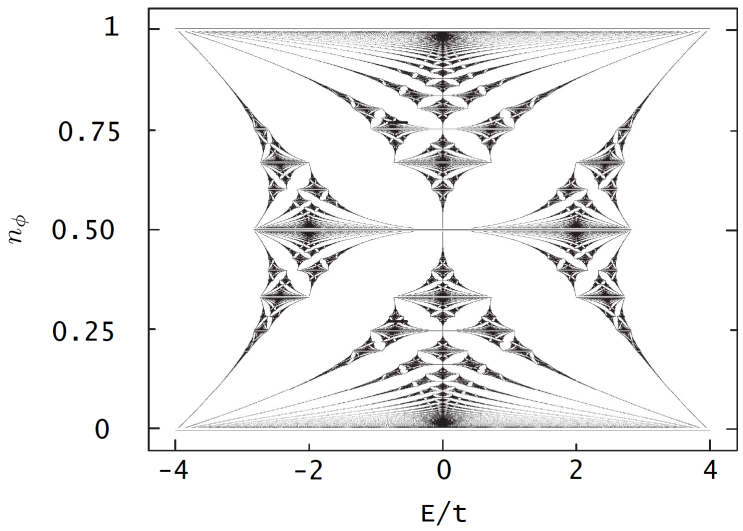

Figure 2.1.: The Hofstadter butterfly plots the flux density n_ϕ vs. the energy eigenvalues of the Hamiltonian 2.31 divided by the hopping factor E/t. The pattern repeats for n_ϕ outside the plotted range [30]. The single energy band (from the zero-field Hamiltonian) splits into q sub-bands if a *rational* flux density $n_\phi = p/q$ is introduced in the system. The figure has been adapted from [34].

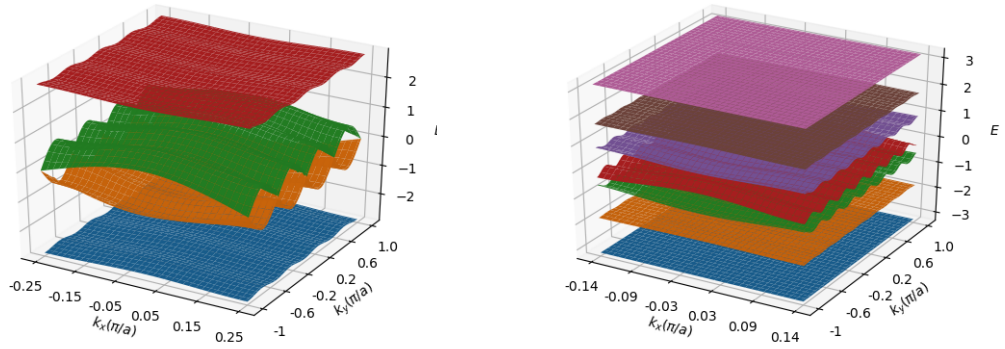

a $n_\phi = 1/4$, $C = 1$ for the lowest band b $n_\phi = 1/7$, $C = 1$ for the lowest band

Figure 2.2.: Energy spectrum of the single-particle Hamiltonian 2.31 for two different flux densities. The Chern number of the lowest band can be tuned by varying the filling factor ν of the system according to Eq. 2.30. We note also that the lowest band is flat and well separated, which makes the Hofstadter model a good candidate for stabilizing FCIs.

2.4.2. Single-particle energy spectrum

If the Hamiltonian is symmetric under translations—in two-dimensions, if the lattice translation operators T_x and T_y (defined along the $x-$ and $y-$axis respectively) commute with each other, and with the Hamiltonian—one can apply the Bloch theorem to obtain a quantized energy spectrum with Bloch energy bands [35] (this is used to solve cases involving periodic potential). The single-particle Hamiltonian 2.31 shows this symmetry in the case of zero magnetic field. If we now introduce a finite magnetic field $\mathbf{B}$ (with vector potential $\mathbf{A}$ in the x-Landau gauge), this translation symmetry of the Hamiltonian is broken, as the vector potential is not invariant under translation by the lattice unit vectors.
Thus to obtain the single-particle energy spectrum, we need to find the symmetries of the Hamiltonian. We can construct new commuting operators that define such a symmetry—these are the *magnetic translation operators* (MTOs) and are a combination of translation and gauge transformations [36]. The magnetic translation algebra is constructed as in [37]. In cases where the magnetic field is homogeneous, the commuting MTOs enclose a *magnetic unit cell*, that—for a given flux density $n_\phi = p/q$—is q times larger than the normal unit cell. The choice of the magnetic unit cell is not unique—we choose a cell oriented along the x-axis, with area $A_{\mathrm{MUC}} = q \times 1$ for unit lattice constant.

We need to solve the Schrödinger equation for the energy spectrum of the single-

particle Hamiltonian in the Hofstadter model. The MTOs can be explicitly written as [36]

$$M_x^q = \sum_{m,n} a^\dagger_{m+q,n} a_{m,n} \quad \text{and} \quad M_y^1 = \sum_{m,n} a^\dagger_{m,n+1} a_{m,n} \tag{2.32}$$

where m and n denote the site indices along the $x-$ and $y-$axes respectively. As these operators commute with each other and with H_0 (by construction), we can define a Bloch theorem for magnetic translation symmetry with the momentum $\mathbf{k}$ lying in the first *magnetic Brillouin zone* such that $-\pi/(qa) \leq k_x < \pi/(qa)$ and $-\pi/a \leq k_y < \pi/a$ [38].

This motivates the wavefunction ansatz

$$\Psi_{m,n} = e^{ik_x ma} e^{ik_y na} \psi_m \tag{2.33}$$

where $\psi_{m+q} = \psi_m$. This ansatz is the magnetic equivalent of the Bloch wavefunction. Inserting this into Eq.2.31, we set up a q-dimensional eigenvalue problem which one solves numerically. The solutions give the single-particle energy spectrum, plotted for some values of n_ϕ in Fig. 2.2.
For a rational flux density $n_\phi = p/q$, the energy spectrum will have q bands—plotting the energy eigenvalues with respect to the flux density n_ϕ generates the Hofstadter butterfly structure in Fig. 2.1. Further, increasing q decreases the band width, such that $n_\phi \to 0$ corresponds to the continuum limit [39]. Moreover the filling factor of the lowest Landau level is given as $\nu = n/n_\phi$, where n is the filling factor of the system.

There are several important advantages of using the Hofstadter model for our research. Firstly, due to the fractal energy spectrum with any desired Chern band, the system is highly configurable and we can easily access all of the desired topological flat bands. As mentioned in 2.3, we require a lowest Chern band with Chern number $|C|$, that is well separated from the higher bands for our investigation of FCIs. We follow [14], where the authors demonstrate that these states are realized in the Hofstadter model for the density of states $n_s = 1/q$. Which corresponds to a flux density of

$$n_\phi = \frac{p}{|C|p - \mathrm{sgn}(C)} = \frac{p}{q} \tag{2.34}$$

for $p, q \in \mathbb{N}$.

Second, the Hamiltonian is computationally minimal, since it only requires nearest-neighbor hopping on a square lattice with a phase factor, albeit with an enlarged effective unit cell.
Third, and crucially for our research, we can tune the relevant length scale in the problem, the magnetic length, simply by adjusting the flux density. This allows

us to access a large selection of system sizes at a low computational cost. We can also choose the magnetic unit cell dimensions to be in the preferred direction for our algorithm, which in our case is the x-direction. This powerful combination of configurability and simplicity make the Hofstadter model an ideal choice for our research.

2.4.3. Interaction Hamiltonian

The many-body Hamiltonian comprises the single-particle Hamiltonian from Eq. 2.31 with the addition of a density-density interaction term, such that

$$H = H_0 + \sum_{\kappa'=1}^{\lceil\kappa\rceil} V(\kappa', n_\phi) f_{\kappa'-1}(\kappa) \sum_{\langle ij\rangle_{\kappa'}} \rho_i \rho_j \tag{2.35}$$

where $\kappa \in \mathbb{R}^+$ is the interaction range, $V(\kappa', n_\phi) = V_0/(\kappa'/l_B)$ is the Coulomb potential accounting for the fact that the lattice constant in units of l_B varies as a function of n_ϕ, $f_i(\kappa) = \min\{\Theta(\kappa - i)(\kappa - i), 1\}$ is a scale factor involving the Heaviside step function Θ, and $\rho_i = c_i^\dagger c_i$ is the fermionic density operator. The sum is constructed such that we can tune the interaction range continuously with respect to κ. In cases where κ is non-integer, we scale the $\lceil\kappa\rceil$th nearest-neighbor term by the fractional part of κ, where $\lceil \dots \rceil$ denotes the ceiling operator. The interaction strength constant, $V_0 = 10$, is chosen predominantly due to its simplicity, and hence low computational expense.

We note that although non-Abelian FQH states were originally introduced via many-body interaction terms, it has since been shown that equivalent phases may also be stabilized with two-body interactions [40–42].

Chapter 3

Methods

In this chapter, we discuss and motivate the numerical methods utilized in our research.
To investigate the physics of quantum many-body systems, we perform large scale numerical simulations. The main difficulty in this investigation has its roots in the exponential scaling of the Hilbert space with the system size - if the single particle Hilbert space is spanned by d states, the basis of the corresponding N-particle Hilbert space comprises of d^N states.

To this end, Matrix product state (MPS) based methods are well established tools for the simulation of quantum many-body systems, notably for systems involving fermionic degrees of freedom (where the otherwise efficient quantum Monte Carlo methods run into the notorious sign problem). The success of these methods can be attributed to the fact that the ground states of interest (in our case, of two-dimensional gapped Hamiltonians) are area law states that only occupy a corner of the Hilbert space.
In Section 3.1, we motivate these methods with a brief discussion of entanglement.

3.1. Entanglement and the area law

When different degrees of freedom of a quantum system cannot be described independently, we say that the system is entangled [43]. A fundamental understanding of this phenomenon proved crucial in the development of numerical methods for the efficient simulation of many-body systems. Furthermore, the classification of topological order—through topological entanglement entropy—is based on this phenomenon [44].
Consider the bipartition of a 1D system into sections A and B, such that $|\psi\rangle \in \mathcal{H} = \mathcal{H}_A \otimes \mathcal{H}_B$, where $\mathcal{H}_{A/B}$ consists of all states described to the left/right of the bond that we choose. For a pure state $|\psi\rangle \in \mathcal{H}$, we define the reduced density matrix of a subsystem (say, A) by tracing out the degrees of freedom of the subsystem B:

$$\rho^A = \mathrm{Tr}_B(|\psi\rangle \langle\psi|) \tag{3.1}$$

We can quantify the entanglement between the two subsystems with the von Neumann entanglement entropy $S = -\mathrm{Tr}(\rho^A \log(\rho^A))$.
If the reduced density matrices on A or B are mixed, it follows that $S \neq 0$ and we say the subsystems are entangled.
Each pure state $|\psi\rangle \in \mathcal{H}$ can be written in terms of the states of the subsystems using the Schmidt decomposition

$$|\psi\rangle = \sum_\alpha \Lambda_\alpha |\alpha\rangle_A \otimes |\alpha\rangle_B \tag{3.2}$$

Where the states $\{|\alpha\rangle_{A/B}\}$ form an orthonormal basis of $\mathcal{H}_{A/B}$, and the Schmidt coefficients $\Lambda_\alpha \geq 0$. For a normalized state $|\psi\rangle$, we find $\sum_\alpha \Lambda_\alpha^2 = 1$.
From Eq. (3.2), we can write $\rho^A = \sum_\alpha \Lambda_\alpha |\alpha\rangle_R \langle\alpha|_R$. Thus the entanglement entropy can be written in terms of the Schmidt values,

$$S = -Tr(\rho^A \log(\rho^A)) = -\sum_\alpha \Lambda_\alpha^2 \log(\Lambda_\alpha^2) \tag{3.3}$$

For the case where there is no entanglement, $\Lambda_1 = 1$, $\Lambda_{n>1} = 0$ and thus $S = 0$. A typical—randomly drawn—state in the Hilbert space follows a volume law; in particular, the entropy $S = \frac{N}{2}\log d - \frac{1}{2}$ is close to the maximum entropy [45] (where d is the on-site Hilbert space dimension). Ground states, on the other hand, have been shown to be area law states—the entanglement entropy S grows proportionally with the area of the cut, and further, $S \propto L^{D-1}$, where L is the length of the system and D is the physical dimension [46].
For the 1D chain shown of size L, it follows that S(L) is constant (for L $>$ ξ, the correlation length of the system). The number of Schmidt values needed increases exponentially with the system size for a randomly drawn state—for one-dimensional area law states, it remains constant (further, only a few Schmidt states contribute significantly, and the singular values in a gapped one-dimensional system often decay exponentially [47]). The MPS representation exploits this property, and provides an efficient way to represent these states [48].

3.2. Matrix Product States

In the MPS ansatz, the coefficients $\psi_{i_1,\ldots,i_N}$ of a pure quantum state are written as products of matrices.

$$\psi_{i_1,\ldots,i_N} = M^{[1]i_1} M^{[2]i_2} \ldots M^{[N]i_N} \tag{3.4}$$

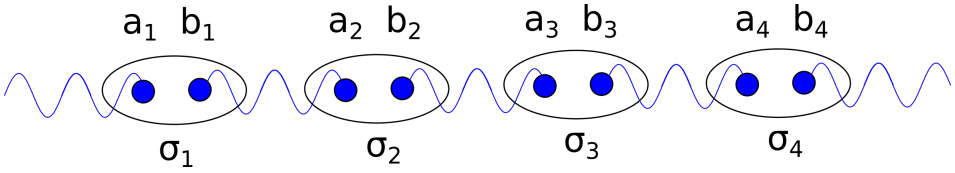

Figure 3.1.: The AKLT state. The ellipses denote the spin-1 states (described in Eq. 3.2.1) σ_i, while the singlet states between neighboring spins-1/2 b_i and a_{i+1} are given by the squiggly lines.

Where $M^{[n]}$ is a set of rank-3 tensors such that $M^{[n]i_n}$ are matrices with dimension $\chi_n \times \chi_{n+1}$. χ_n is the bond dimension of bond n. Further, $\chi_1 = \chi_{N+1} = 1$ such that the matrix product returns a number. We also introduce a diagrammatic representation (See Fig. 3.2) for tensor networks, where a tensor with n indices is represented by a symbol with n legs—further, one can perform tensor contraction by connecting two legs. Note that the choice of symbol is arbitrary (here we represent all tensors with a square), and the tensor is identified by the number of legs it has.

3.2.1. Example: AKLT state

We discuss the spin-1 Affleck-Kennedy-Lieb-Tasaki (AKLT) state [49] because it presents a analytically solvable example. The AKLT state is the ground state of the spin-1 Hamiltonian on a chain (See Fig. 3.1)

$$H = -\sum_i \mathbf{S}_i \cdot \mathbf{S}_{i+1} + \frac{1}{3}(\mathbf{S}_i \cdot \mathbf{S}_j)^2 \tag{3.5}$$

where $\mathbf{S}$ are spin-1 operators. In the ground state, each spin-1 site is described in terms of the triplet states of two spins-1/2:

$$\begin{aligned} |+\rangle &= |\uparrow\uparrow\rangle \\ |0\rangle &= \frac{|\uparrow\downarrow\rangle + |\downarrow\uparrow\rangle}{\sqrt{2}} \\ |-\rangle &= |\downarrow\downarrow\rangle \end{aligned}$$

Adjacent spins-1/2 of neighboring sites form a singlet state $\frac{|\uparrow\downarrow\rangle - |\downarrow\uparrow\rangle}{\sqrt{2}}$. One finds that this state can be written as an MPS of dimension 2. Consider first the singlet state on bond i

$$|\Sigma^{[i]}\rangle = \sum_{b_i, a_{i+1}} \Sigma_{ba} |b_i\rangle |a_{i+1}\rangle \tag{3.6}$$

with matrix Σ

$$\Sigma = \begin{pmatrix} 0 & \frac{1}{\sqrt{2}} \\ -\frac{1}{\sqrt{2}} & 0 \end{pmatrix} \tag{3.7}$$

for b_i and a_{i+1} as the adjacent spin-1/2 degrees of freedom on site i and $i+1$ respectively. The ground state, written in terms of the spins-1/2 is then:

$$|\psi_{GS}\rangle = \sum_{a,b} \Sigma_{b_1 a_2} \Sigma_{b_2 a_3} \dots \Sigma_{b_L a_1} |\boldsymbol{ab}\rangle \tag{3.8}$$

We now introduce a mapping from the states of two spins-1/2 on site i, $|a_i\rangle |b_i\rangle \in \{|\uparrow\rangle, |\downarrow\rangle\}^{\otimes 2}$ to spin-1 states $|\sigma_i\rangle \in \{|+\rangle, |0\rangle, |-\rangle\}$, with $M^{\sigma}_{ab} |\sigma\rangle \langle ab|$. $M^{\sigma}_{ab} |\sigma\rangle \langle ab|$ can be written in terms of three 2×2 matrices, one for each value of σ

$$M^{+} = \begin{pmatrix} 1 & 0 \\ 0 & 0 \end{pmatrix}, M^{0} = \begin{pmatrix} 0 & \frac{1}{\sqrt{2}} \\ \frac{1}{\sqrt{2}} & 0 \end{pmatrix}, M^{-} = \begin{pmatrix} 0 & 0 \\ 0 & 1 \end{pmatrix}. \tag{3.9}$$

The mapping for the full chain of length L is

$$\sum_{\sigma,a,b} M^{\sigma_1}_{a_1 b_1} M^{\sigma_2}_{a_2 b_2} \dots M^{\sigma_L}_{a_L b_L} |\boldsymbol{\sigma}\rangle \langle \boldsymbol{ab}| \tag{3.10}$$

Applying this to the ground state (consisting of singlet states on every bond) written in terms of the spin-1/2 states, we obtain the form

$$|\psi\rangle = \sum_{\boldsymbol{\sigma}} \mathrm{Tr}(M^{\sigma_1} \Sigma M^{\sigma_2} \Sigma \dots M^{\sigma_L} \Sigma) |\boldsymbol{\sigma}\rangle \tag{3.11}$$

Identifying $A^{\sigma} = M^{\sigma} \Sigma$ gives us the MPS form of the AKLT state.
We note that any state in a finite system can be represented exactly in the MPS ansatz. However, for a volume law state, the bond dimension χ required increases exponentially with the number of sites N—area law states on the other hand can be well approximated with a finite bond dimension.

3.2.2. Canonical form

As we wish to discuss numerical techniques in the MPS framework, we introduce the *canonical form* of MPS states—in these forms, all tensors (except one) are unitary. First, we note that the MPS representation is not unique. In particular for a bond in an MPS (say, between sites n and $n+1$), we can carry out the substitutions

$$M^{[n] j_n} \to \tilde{M}^{[n] j_n} = M^{[n] j_n} V^{-1} \tag{3.12}$$

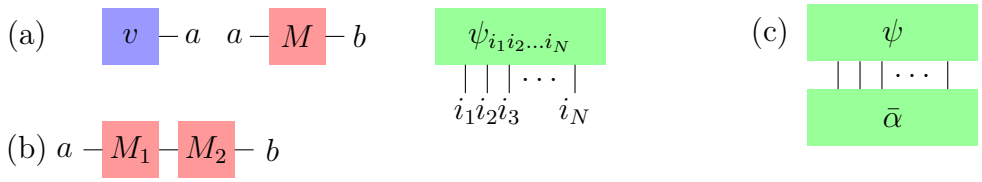

Figure 3.2.: (a) Graphical notation for representing tensor networks—in particular for vector v, matrix M and wavefunction $|\psi\rangle$ consisting of N sites. (b) We perform tensor contraction by joining two legs, here $(M_1M_2)_{ab} = \sum_i (M_1)_{ai}(M_2)_{ib}$. (c) Representation of the overlap $\langle\alpha|\psi\rangle$ between wavefunctions ψ and α.

$$M^{[n+1]j_{n+1}} \to \tilde{M}^{[n+1]j_{n+1}} = V M^{[n+1]j_{n+1}} \tag{3.13}$$

for an invertible matrix V with dimension $\chi_{n+1} \times \chi_{n+1}$, and this would describe the same state as before. We can exploit this to obtain a convenient form—the canonical form—of the MPS. For a general MPS state with rank-3 tensors $M^{[n]j_n}$, one can decompose the tensors as $\tilde{M}^{[n]j_n} = \Gamma^{[n]j_n}\Lambda^{[n+1]}$ where Λ is a diagonal square matrix consisting of positive terms, that correspond to the Schmidt values at the bond. This form also allows us to choose the normalization. Consider the following kinds of grouping

$$A^{[n]j_n} = \Lambda^{[n]}\Gamma^{[n]j_n} \tag{3.14}$$

$$B^{[n]j_n} = \Gamma^{[n]j_n}\Lambda^{[n+1]} \tag{3.15}$$

We can show that the A-(B-) form consists of left- (right-)normalized matrices. Further, we can define a *mixed canonical form*, where we group the Γ and Λ matrices in a way that gives A-matrices to the left of some bond n and B-matrices to the right. This is crucial for implementing DMRG, and is discussed in Section 3.3.

3.2.3. Matrix product operators

Finally, let us look at the operator counterparts to the MPS. These are termed *Matrix Product Operators* (MPOs), and consist of rank-4 tensors with two physical indices σ_i and σ_i' (represented as the outgoing and ingoing legs) that represent the on-site degrees of freedom, and two virtual indices that connect horizontally. A general MPO is written as

$$O = \sum_{\sigma,\sigma'} W^{\sigma_1\sigma_1'} W^{\sigma_2\sigma_2'} \dots W^{\sigma_{L-1}\sigma_{L-1}'} W^{\sigma_L\sigma_L'} |\sigma\rangle \langle\sigma| \tag{3.16}$$

We refer to [50] for a procedure by which to construct an MPO form for a Hamiltonian of interest. As an example, a Hamiltonian with multiple one and two-body interactions of the form of $X_i + Y_i Z_{i+1}$ can be written in an MPO form with the following on-site matrices

$$W^{[i]} = \begin{pmatrix} \mathbb{1} & 0 & 0 \\ Z_i & 0 & 0 \\ X_i & Y_i & \mathbb{1} \end{pmatrix} \tag{3.17}$$

3.3. Density Matrix Renormalization Group

In the previous section, we introduced an ansatz that efficiently represents one-dimensional ground states (as these are area law states). In this section we describe a powerful numerical method—called the density matrix renormalization group (DMRG)—that we used in our research to compute ground states and their energies. The approach was initially described by White [51] and later on, was reformulated as a variational optimization scheme within the space of MPS wavefunctions [52]. We consider and describe the latter approach in this section.

3.3.1. Mathematical formulation

Formally stated, the problem is to find a wavefunction $|\psi\rangle$ that minimizes the energy expectation value

$$E = \frac{\langle\psi| H |\psi\rangle}{\langle\psi|\psi\rangle} \tag{3.18}$$

In the following discussion, we reformulate the problem 3.18 to motivate the implementation of DMRG, which we discuss in Section 3.3.2.
We interpret 3.18 as minimizing the expectation value $\langle\psi| H |\psi\rangle$ with the constraint $\langle\psi|\psi\rangle = 1$. Here, we introduce a Lagrange multiplier to extremize functional f:

$$f[|\psi\rangle] = \langle\psi| H |\psi\rangle + \lambda(1 - \langle\psi|\psi\rangle) \tag{3.19}$$

The extremization of this functional can be carried out over the entire system—however, such approaches are often unstable. In DMRG, one localizes this extremization—that is, one optimizes a single MPS tensor at a time.
Starting from an MPS representation of the right-hand side of Eq. 3.19, we contract the tensors around the MPS tensor of site i into H_i and N_i. We can now write the parameters of the MPS tensor of site i in terms of a vector a_i

$$f_i[a_i] = {a_i}^\dagger H_i a_i + \lambda[1 - {a_i}^\dagger N_l a_i] \tag{3.20}$$

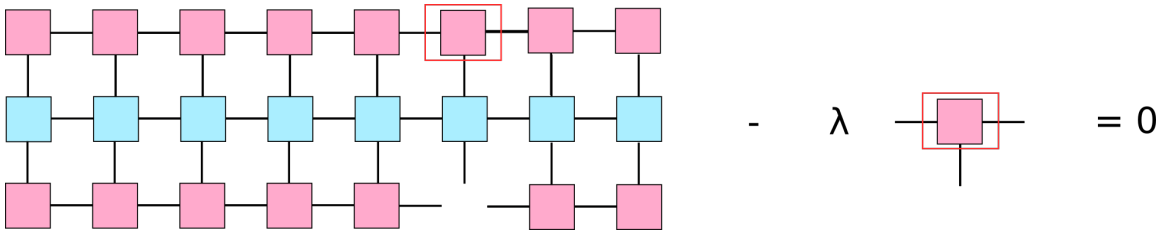

Figure 3.3.: The optimization problem is reduced to N eigenvalue problems. Depicted is one such equation, which corresponds to one iterative step of the DMRG algorithm. The tensor boxed in red is the tensor optimized in this step.

We motivate the mixed canonical form of the MPS. Starting with MPS in the canonical form, we group the tensors such that they are *left normalized* to the left of site i : $A^{j<i} = \Lambda^j \Gamma^j$ and right normalized to the right of site i : $B^{j>i} = \Gamma^j \Lambda^{j+1}$. We also introduce an **on-site** tensor $M^i = \Lambda^i \Gamma^i \Lambda^{i+1}$. In this form, the operator $N_i = \mathbb{1} \ \forall \ i$. For the final step in the optimization procedure, we minimize the functional with respect to $a_i^\dagger$.The problem thus reduces to an eigenvalue equation

$$H_i a_i = \lambda a_i \tag{3.21}$$

3.3.2. Implementation

Before starting the iterative procedure, we transcribe the initial wavefunction—a guess for the ground state—into canonical MPS form and the corresponding Hamiltonian into matrix product operator [2](MPO) form.
The algorithm *sweeps* to the right through sites $i = 1$ to N, in the following manner:
1. Convert MPS to its mixed canonical form, with the on-site tensor M^i.
2. Reshape the on-site tensor into a vector $\boldsymbol{a_i}$, and reshape the contracted tensor H_i into a matrix.
3. Solve the eigenvalue problem 3.21, for instance with the Lanczos algorithm. The equation is depicted graphically in Fig. 3.3. Store the lowest eigenvalue λ as the best guess for the ground state energy.
4. Reshape a_i into an MPS tensor, and convert MPS into mixed canonical form—this time, with the on-site matrix at the next site.
An iterative procedure consisting of many sweeps, from the left to the right and back, is used. The algorithm continues the run until some convergence criterion is satisfied—such as convergence of energy.

3.3.3. iDMRG and two-dimensional systems

In contrast to the finite-size DMRG algorithm that we introduced, the infinite-size version (termed *iDMRG*) grows the system by adding sites to the lattice in the center, and minimizes the MPS wavefunction ansatz with respect to the Hamiltonian for the enlarged system in every iteration [52].
The crucial step in the algorithm involves an assumption of translational invariance—justified in the thermodynamic limit—which motivates a guess wavefunction for each iteration, with the matrices associated with the added sites written in terms of the site matrices of previous iterations. The algorithm then proceeds iteratively, growing the system and minimizing the energy in each step until the matrices in the center converge to a certain point.

The iDMRG algorithm in our research is set on an infinite cylinder geometry that possesses a finite circumference L_y [53], with the infinite length of the cylinder along the x-axis.

Assuming that our state is translationally invariant, with a unit cell of length $\bar{L}$ (for a flux density $n_\phi = p/q$, $\bar{L}$ will be a multiple of q), we can express the infinite MPS with $\bar{L}$ tensors $\{M^{[0]}, M^{[1]}, \ldots, M^{[\bar{L}]}\}$ such that $M^{[i]} = M^{[i+\bar{L}]}$.

DMRG is inherently a 1D method—we can study 2D systems by mapping our system to a 1D system with long-range interactions. This mapping is depicted graphically for the infinite cylinder in Fig. 3.4—note the periodic boundary conditions along the circumference. Along the cylinder axis we assume translational invariance. We employ this geometry to study FQH states in Chapter 4. In Chapter 4 we also discuss the benefits and shortcomings of the algorithm and the infinite cylinder geometry for our research.
We refer the reader to [52] for an involved discussion of iDMRG.

3.4. Characterizing topological order

A significant challenge we faced in our research was the task of identifying *outliers*—computed ground states that are not topological in nature, or have significant finite size effects.
In this section, we discuss the various techniques that were used to confirm the topological nature of the computed ground states and further, to characterize their topological order.

3.4.1. Flux insertion

In this method, we insert magnetic flux Φ_x adiabatically through the longitudinal axis of our infinite cylinder (see Fig. 3.5a) and compute $\langle Q_L \rangle$, the average charge on the left half of the infinite cylinder.

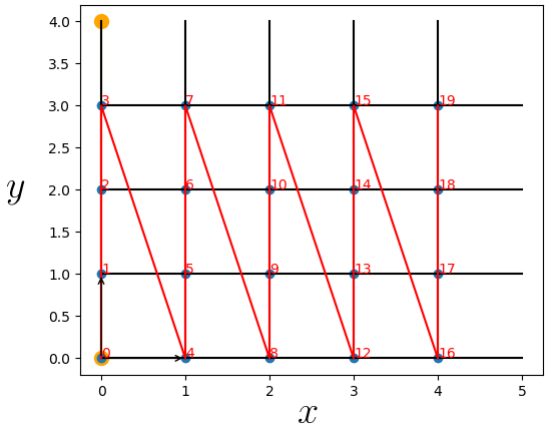

Figure 3.4.: Winding a 1D chain around the infinite cylinder allows us to study the 2D system using DMRG.

We recall that for a FQH state with filling fraction ν and Chern number (for the lowest band) C, the Hall conductivity is given as $\sigma_H = C\nu e^2/h$, where e is the electronic charge and h is Planck's constant. From Laughlin's charge pumping argument, we can show that for a FQH state with $\nu = p/q$, inserting q flux quanta adiabatically causes charge $\Delta Q = q\sigma_H h/e = Cpe$ to be pumped along the cylinder—this provides a way to confirm the FQH nature of our states [31].

3.4.2. Momentum-resolved entanglement spectrum and CFT edge counting

We recall that the iDMRG algorithm solves iteratively for the ground state, by carrying out Schmidt decomposition of the system into two half infinite cylinders and truncating it at a given bond dimension χ.
The *entanglement spectrum* $\{\epsilon_\alpha\}$ is defined in terms of the spectrum $\{\Lambda_\alpha^2\}$ of the reduced density matrix of equation 3.3 by $\Lambda_\alpha^2 = \exp(-\epsilon_\alpha)$ for each α [54]. The translational symmetry T_y of the cylinder allows us to assign momentum quantum numbers to Schmidt states. In momentum-resolved entanglement spectrum, the horizontal axis represents the momentum of the corresponding eigenvector of the reduced density matrix ρ [55].
We consider the $U(1)$ charge symmetry of the Hofstadter Hamiltonian, which allows us to further resolve the spectrum into distinct $U(1)$ charge sectors of the left Schmidt states. Using the low-lying energies in the spectrum, we can comment on the counting of the edge states (see Fig. 3.5b) by comparing them to the characteristic counting of the edge conformal field theory (CFT) [55]—further

characterizing, and confirming the topological nature of our states.

3.4.3. Density profile and correlation functions

We examine the *density profile* $\langle \rho_i \rangle$—the expectation value of the total number operator. This method is powerful for identifying competing phases in our system (such as the Wigner crystal [21]) and finite size effects that could lead to errors in our computation of the topological entanglement entropy. We consider an example for the Laughlin wavefunction in Fig. 3.5c.
We define the *two-particle correlation function* as the expectation value of the density operator ρ of a particle at site 0 with the density operator of a particle at site i:

$$\langle : \rho_0 \rho_i : \rangle = \langle : c_0^\dagger c_0 c_i^\dagger c_i : \rangle \tag{3.22}$$

Computing this quantity for our ground states, we observe a hole at small inter-particle distance $\mathbf{d}$ (because of Pauli's exclusion principle, as we consider fermions in this example). On increasing $\mathbf{d}$ we observe damped oscillations, finally reaching an asymptotic value that characterizes a homogenous fluid. This is consistent with the Laughlin state, a liquid with short-range interactions that effectively maximize the distance between particles. For a theoretical motivation we refer to [56, 57].

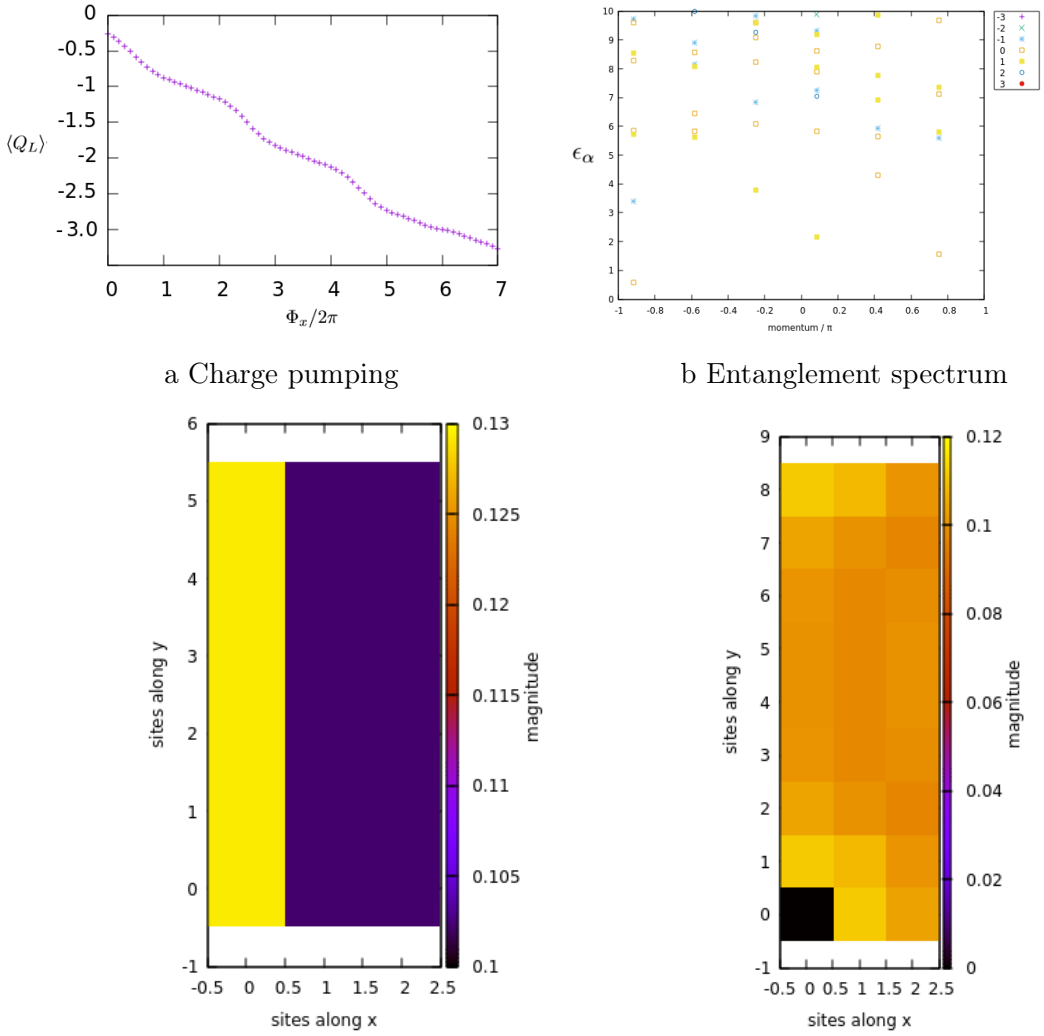

a Charge pumping

b Entanglement spectrum

c Density profile

d Correlation function

Figure 3.5.: (a) Average charge on the left cylinder $\langle Q_L \rangle$ as a function of external flux Φ_x, adiabatically inserted along the longitudinal axis of the cylinder. We consider a state with $\nu = 1/7$ and Chern number 3. The observed charge pumping of three charges with the insertion of seven flux quanta confirms the FQH state.
(b) Momentum-resolved entanglement spectrum for a state with $\nu = 1/3$. Entanglement energies ϵ_α are plotted as a function of the momentum eigenvalues of the Schmidt states, and the color corresponds to the respective $U(1)$ charge sector. One observes an edge counting of (1,1,2,3...), consistent with the edge counting for an Abelian state from CFT. (c) Density profile for an FQH system with $\nu = 1/3$. We consider a system with 2 particles. As each electron splits into three Laughlin quasi-electrons, we observe six density peaks of equal amplitude. (d) The correlation function profile is consistent with the Laughlin state [56]. We note that a larger system size would allow us to better resolve the profile. See Fig. 4.2(d) for such a case.

Chapter 4

Abelian topological order of FQH states in lattice models

Fractional excitations of the ground state, known as anyons, are among the defining features of FQH states. These anyons can obey either Abelian or non-Abelian exchange statistics, such that the fractional phase shift to the ground state wavefunction is given by a one-dimensional or higher-dimensional braid group respectively. [58–62].
In this chapter, we describe our numerical investigation of the topological order and corresponding ground state statistics of the single-component $\nu = 2/5$ and $3/7$ FQH states, and present the results and analysis of our research.

4.1. Overview of current FQH research

In this section, we motivate the current state of research on the topological order of FQH states. Here, we build up on the introduction contained in Chapter 1.

Continuum FQH states in the Jain hierarchy have been shown numerically [63–65], and for the Laughlin state also experimentally [24, 25], to possess Abelian topological order for the Coulomb interaction. The analysis of corresponding lattice FQH states on the other hand is complicated by several factors, including the limited number of viable experimental systems [66], and the difficulty of engineering long-range interactions [67].
It has also been shown that the lattice can host fundamentally different phases of matter [68], as well as states with non-Abelian statistics at equivalent filling factors [41, 69]. In particular, there are Abelian FQH states in lattice models stabilized by two-body interactions that have been shown to possess non-Abelian statistics when interactions are sufficiently long-range [41], which provides motivation for further study.
Given the experimental challenges and theoretical interest, it is important to develop an efficient method to analyse such states numerically and probe their quantum statistics.

4.2. Identifying topological order

In our research, we performed large-scale numerical calculations using the iDMRG algorithm to investigate the Abelian nature of the single-component $\nu = 2/5$ and $3/7$ FQH states in the Hofstadter model with a large interaction strength, chosen such that inter-band transitions are likely to occur.

For the purposes of this project, the iDMRG algorithm offers both notable advantages, as well as some drawbacks. The main advantage is that, unlike exact diagonalization, no band projection needs to be taken for the interaction Hamiltonian and so inter-band transition effects are automatically taken into account. An added benefit is that the algorithm works in the semi-thermodynamic limit, meaning that a thermodynamic limit ansatz is taken along the the cylinder axis. Furthermore, the system sizes attainable along the circumference are highly competitive with alternative methods. The major disadvantage of the algorithm is that it is inherently one dimensional, which means that even modest interaction ranges on the two-dimension surface correspond to exponentially long-range interactions on the unraveled one-dimensional chain. This is particularly an issue for this project as we are motivated to tune the interaction range. Nevertheless, we overcome this barrier through the use of an optimal sampling algorithm, as explained in later sections.

The identification of the Abelian topological order in our research is based on the area law of entanglement $S = \alpha L_y - \gamma + O(e^{-L})$, where S is the von Neumann entanglement entropy, α is a non-universal constant dependent on the microscopic parameters of the Hamiltonian, L_y is the circumference of our cylinder and γ is the topological entanglement entropy [44, 70].

Thus, we use the iDMRG algorithm on an infinite cylinder to compute ground states with different L_y. We compute the von Neumann entanglement entropy (see Eq. 3.3) at various system sizes to construct detailed plots of the area law of entanglement, and extrapolate to obtain γ as the intercept at the ordinate.
The topological entanglement entropy cannot be removed by reducing the system size and depends intrinsically on the type of quasiparticle excitations hosted by the ground state. It is given as $\gamma = \ln(D)$, where $D = \sqrt{\sum_a d_a}$ is the total quantum dimension of the field theory description and d_a is the quantum dimension of a quasiparticle of type a. The quantum dimension for Abelian anyons is always one, whereas for non-Abelian anyons $d_a > 1$ [44]. The conventional Laughlin argument for an Abelian FQH state at filling $\nu = r/s$ is that the ground state degeneracy is s, the quasiparticles possess $1/s$ of an electronic charge, and the topological entanglement entropy is $\gamma = \ln(\sqrt{s})$ [8, 71]. For non-Abelian order, this value is always larger. We note, however, that it has been recently shown that the topological entanglement entropy may be larger than $\ln(\sqrt{s})$ even for single-component Abelian states, taking the general form $\gamma = \ln(\sqrt{\lambda s})$, with $\lambda \in \mathbb{Z}^+$

[72, 73]. Thus the original statement $\ln(\sqrt{s})$ implies that the state is Abelian, though the converse is not always true. By precisely extrapolating the value of the topological entanglement entropy from the area law of entanglement, we are able to definitively conclude that a state exhibits Abelian order when $\gamma = \ln(\sqrt{s})$.

Although the premise is simple, the execution is fraught with potential problems. The first and perhaps most apparent problem is the precision to which we are able to extrapolate to the topological entanglement entropy. In many-body numerics, such as iDMRG, we are restricted to relatively small system sizes. Not only is the area law technically non-linear at small system sizes, but more importantly, finite-size effects exist along with this, leaving the area law data highly spread and unreliable. Second, the individual data points are computed at a finite bond dimension, which may be significantly distant from the actual value in the $\chi \to \infty$ limit. Even slight errors in the individual data points can have a compound effect on the total error of the topological entanglement entropy, particularly if the points are close together on the L-axis. Further, there is an arbitrariness in how to construct the line of best fit—which points should be included and which ones should be left out? We observed that minor changes in acceptance criteria can have a drastic impact on the slope and the y-intercept of the linear regression. Although a lot has been achieved with such computations in the past few years [31, 74, 75], we argue that in order to perform a stand-alone computation of the topological entanglement entropy, more care is required to address numerical and statistical errors.

In our research, we address these issues by devising a systematic method that is reliable enough to accurately compute the topological entanglement entropy for $\nu = 1/3$ and $2/5$ states. Further, using this method we obtain an estimate for the topological entanglement entropy of the $\nu = 3/7$ state.

First, we plot the area law of entanglement in units of magnetic length, which in the square-lattice Hofstadter model depends on the flux density through $L_y/l_B = \sqrt{2\pi n_\phi} L_y$. Since the processing cost for convergence for iDMRG scales exponentially with L_y, exploiting the natural length scale of the Hofstadter model allows us to obtain a larger number of data points at relatively low computational cost [74]. Second, to remove arbitrariness and optimize the flux densities considered, we choose values guided by an algorithm (this is detailed in the Appendix A). For each data point, we scale the computation of the entanglement entropy with bond dimension to obtain an extrapolation with error in the $\chi \to \infty$ limit. We accept data points only if the error is smaller than 0.1%. Finally, to mitigate finite-size effects, we construct multiple lines of best fit as we incrementally exclude data in ascending L_y/l_B, and stop as soon as the linear regression of the remaining points yields $R^2 > 0.99$. This is a necessary compromise between a precisely straight line and a maximal data set. The details of the numerical method are discussed in the

Appendix A.

4.3. Results

In this section we present our results from the many-body numerical calculations. In section 4.3.1 we demonstrate the Abelian statistics of the FQH states in the case of nearest-neighbor interactions, and in sections 4.3.2 and 4.3.3 we analyse the effect on the topological entanglement entropy as we tune the interaction range and strength respectively.

4.3.1. Nearest-neighbor interactions

To begin, we consider the FQH states stabilized by nearest-neighbor interactions, as defined in the interaction Hamiltonian with $\kappa = 1$.
To benchmark our results, we start with the Laughlin filling $\nu = 1/3$. Although this state has been previously investigated using an area law constructed from a many-body lattice simulation [31, 74, 75], we emphasize that the cited investigations are not systematic enough to be transferable for higher-order states in the hierarchy. We therefore present the computation of the $\nu = 1/3$ area law plot using our systematic procedure in Fig. 4.1. We have algorithmically chosen our data points to avoid selection bias, we have scaled each data point with χ to eliminate convergence error, and we have systematically excluded small-L_y/l_B data to alleviate finite-size effects. Most importantly, all points are converged in the entanglement entropy to $\delta S < 0.1\%$, have a spacing of $\Delta(L_y/l_B) > 0.1$, and the linear regression staisfies $R^2 > 0.99$. Further tightening the constraints of the algorithm yields eight such points, shown in the figure.

We note that for the $\nu = 1/3$ state we obtained significantly more data points that satisfy all of the criteria, which is why we further restricted the algorithm to yield a smaller representative sample. The topological entanglement entropy obtained from this data is $\gamma = 0.557 \pm 0.043$, which agrees closely with the Abelian theory value of $\gamma = \ln(\sqrt{3}) \approx 0.549$ [76].

We progress from the Laughlin state to the next filling fraction in the hierarchy: $\nu = 2/5$. We hold the $\nu = 2/5$ data to the same stringent quality standards that we enforced for the $\nu = 1/3$ state. The data obtained are shown in Fig. 4.1(b), which serves as our first original result. Since for the $\nu = 2/5$ state it is more difficult to satisfy configuration constraints and convergence at accessible χ, this presents a significant computational challenge compared to the Laughlin state [77]. Nevertheless, we obtain a set of four data points that satisfy all of the criteria. The topological entanglement entropy obtained from these data is $\gamma = 0.850 \pm 0.103$, which agrees with the Abelian theory value of $\gamma = \ln(\sqrt{5}) \approx 0.805$ and iDMRG

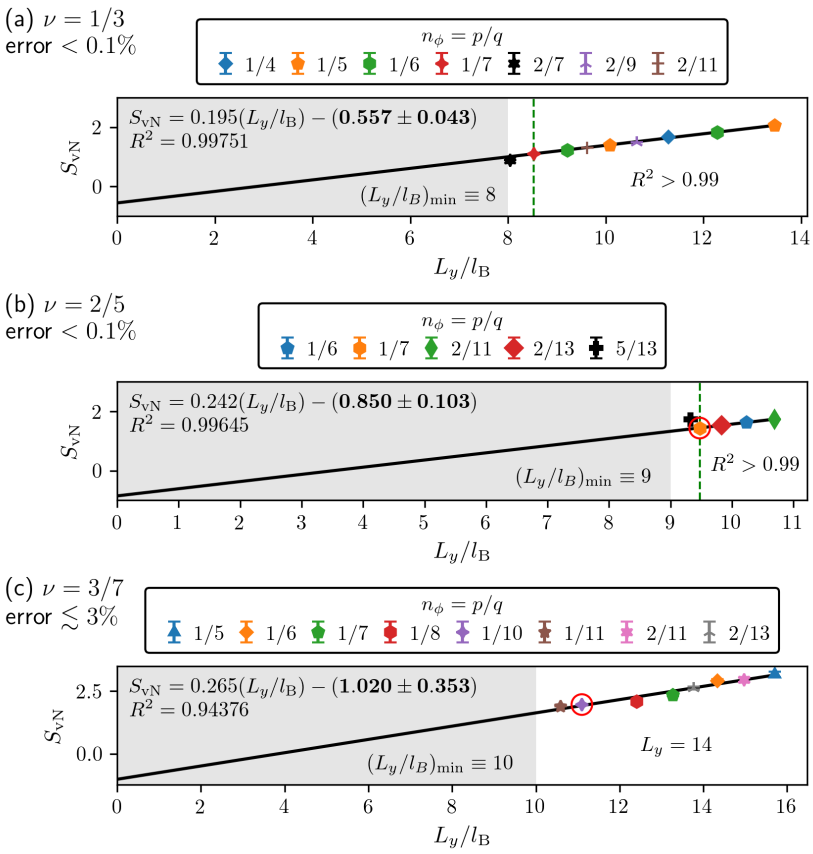

Figure 4.1.: Von Neumann entanglement entropy, S_{vN}, against cylinder circumference, L_y, in units of magnetic length, $l_B = (2\pi n_\phi)^{-1/2}$, for the fermionic hierarchy states at (a) $\nu = 1/3$, (b) $\nu = 2/5$, and (c) $\nu = 3/7$. In each case, we use nearest neighbor interactions ($\kappa = 1$). (a, b) The threshold where the R^2 value first exceeds 0.99 is marked with a green dashed line. All of the points above this threshold are used to construct the line of best fit. In (c), we present the compete data set with our largest system size $L_y = 14$. In all cases, we obtain points based on the systematic procedure outlined in Appendix A with $\chi_{max} = 3000$. The complete data sets are shown in the Appendix (in Fig. B.1) and the points circled in red are studied in Fig. 4.2.

computations using the V_1 Haldane pseudopotential [78]. Moreover, it is well-separated from the non-Abelian prediction of $\gamma = \ln(\sqrt{5(\phi^2+1)}) \approx 1.448$, where ϕ is the golden ratio [71, 79].

There are several additional remarks that can be made, specifically in comparision to the Laughlin state. First, the minimum L_y/l_B to effectively eliminate

finite-size effects is larger for the $\nu = 2/5$ state than for $1/3$, increasing from 8.5 to 9.5. Second, the average spacing of the data on the L_y/l_B-axis is reduced. States with a larger cylinder circumference are generally more expensive to converge, and so we were not able to access high-L_y/l_B states with such stringent precision. Finally, although this figure shows all of the data points obtained in accordance to the algorithm, we generally obtained a vast set of data that corroborate this conclusion. The Appendix A also explains how one may haphazardly reach the same conclusion when not following a rigorous procedure.
The last filling factor that we consider is the $\nu = 3/7$ state where, unlike in the previous cases, the area law has not been previously investigated in any form. As before, we systematically select flux densities guided by our algorithm and we scale each configuration with χ so that we can extrapolate to the $\chi \to \infty$ limit. Due to computational expense of the $\nu = 3/7$ configurations, we are not able to converge every data point to within $< 0.1\%$ error and so we cannot directly use the R^2 value as an indicator of finite-size effects. Instead, we present the data for the largest system sizes that we examined ($L_y/l_B > 10$ and $L_y = 14$) with $\lesssim 3\%$ error in Fig. 4.1(c). The full data set is shown in the Appendix (in Fig. B.1).
Interestingly, we note that there are two types of finite-size effects in the problem. Not only is there a finite-size effect due to cylinder circumference in units of magnetic length, the physical length scale in the system, but there is also a finite-size effect due to the cylinder circumference alone, the numerical length scale. Although a large L_y/l_B ensures that each FQH droplet has a large allocated area, a large L_y additionally ensures that there are enough sites (matrices in the MPS) in the finite direction of the algorithm to accurately represent the ground-state wavefunction. Since an increase in L_y/l_B coarsely corresponds to an increase in L_y, this is an effect that was not apparent in the previous two states. In line with the observed trend, we obtain a topological entanglement entropy of $\gamma = 1.020 \pm 0.353$,which is in agreement with the Abelian theory value of $\gamma = \ln(\sqrt{7}) \approx 0.973$, and well-separated from the non-Abelian prediction of $\gamma = \ln(\sqrt{7(\phi^2+1)}) \approx 1.616$ [79–82]

To confirm the FQH nature of the configurations, we additionally examine each data point in detail. We present the case studies for the red-circled points in Fig 4.1. We examine the details of the $\nu = 2/5$ configuration at $n_\phi = 1/7$ and (L_x, L_y) = (1,10), shown in Fig. 4.2.(a-d), and subsequently the $\nu = 3/7$ configuration at $n_\phi = 1/10$ and $(L_x, L_y) = (1, 14)$, shown in Fig. 4.2.(e-h). In Fig. 4.2.(a) we present the charge pumping (see section 3.4.1) of the $\nu = 2/5$ configuration. The charge pumping shows that two charges are pumped across the cut after an insertion of five flux quanta, which confirms the $\nu = 2/5$ FQH state. In Fig. 4.2.(b), we present the momentum-resolved entanglement spectrum discussed in section 3.4.2. For the $\nu = 2/5$ Jain state, the counting is governed by the CFT for two non-interacting chiral bosons, which yields 1,2,5,10,... with a multi-branch

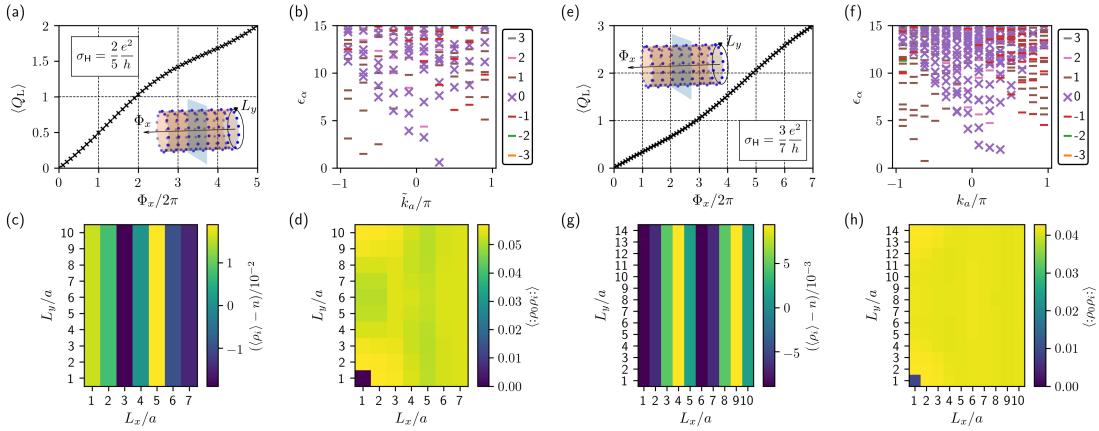

Figure 4.2.: Case studies of the points circled in red from Fig. 4.1. The $\nu = 2/5$ state is obtained at $n_\phi = 1/7, (L_x, L_y) = (1, 10)$,and $\chi = 800$. The $\nu = 3/7$ state is obtained at $n_\phi = 1/10, (L_x, L_y) = (1, 14)$, and $\chi = 2000$.
(a, e) Average charge on the left half of the cylinder, $\langle Q_L \rangle$, as a function of the external flux, ϕ_x, adiabatically inserted along the cylinder axis as shown in the inset (not to scale). The charge pumping was performed at the reduced bond dimensions of $\chi = 400$ and 500, respectively. (b, f) Momentum-resolved entanglement spectrum, showing the entanglement energies, ϵ_α as a function of the momentum eigenvalues of the Schmidt states (see section 3.4.2). In (b), we shift the spectrum, such that $k_a \to \tilde{k}_a$, to emphasize the edge modes.
(c, g) Average density, $\langle \rho_i \rangle$, and (d, h) two-point correlation function, $\langle : \rho_0 \rho_i : \rangle$, for each site in the MPS unit cell. Note that the dimensions of the MPS unit cell are given in units of the lattice constant in this figure.

structure [83, 84].

We note that we are unable to resolve the multi-branch structure in Fig. 4.2.(b) and the verification of the counting sequence is hindered due to the modest momentum resolution, the compactified cylinder geometry, and the fact that post-Laughlin Jain states are not pure CFT states [85]. We see that the first two edge degeneracies are resolved for the bottom branch, 1,2,..., which shows similar energy gaps to the literature [85] and tentatively accords with the Abelian Jain state. However, we emphasize that the optimal configurations for the area law plot, studied in our research, are not the optimal configurations to elucidate the edge counting.
Finally in Fig. 4.2.(c,d) we plot the density and two particle correlation function,

which we have described in section 3.4.3. The density plot shows that we are in a striped phase and the two-point correlation function has the expected form for a conventional FQH state [39, 57, 74]. Most significantly, we can see from the asymmetric density and slight interference in the correlation function profile that, despite our best efforts, some minor finite-size effects still remain. In Fig. 4.2.(e), we present the analogous charge pumping curve for the $\nu = 3/7$ configuration. In this case, we observe three charges pumped after an insertion of seven flux quanta, again in agreement with the expected Hall conductivity for the $\nu = 3/7$ FQH state in a $C = 1$ band. In Fig. 4.2(f), we show the momentum-resolved entanglement spectrum, now at the higher resolution of $L_y = 14$. In this case we are only able to accurately resolve the first degeneracy of the bottom branch to be 1 and hence the verification of edge-state counting is ambiguous [83]. Reassuringly, the density and two-point correlation function profiles in Fig. 4.2.(g,h) show less influence of the finite system size than the $\nu = 2/5$ configuration. The FQH configuration is again in a striped phase and shows the conventional correlation function profile.

4.3.2. Tuning interaction range

Having observed Abelian topological order for the $\nu = 1/3$, $2/5$ and $3/7$ states when stabilized by a nearest-neighbor density-density interaction term, we now investigate the effect of increasing the interaction range, such that $1 \leq \kappa \leq 3$. As before, we start with the most prominent $\nu = 1/3$ state.

In order to investigate the effect of tuning interaction range, we take the eight accepted points in Fig. 4.1.(a). Subsequently, we construct equivalent area law plots for up to third nearest-neighbor interactions, as shown in Fig. 4.3.(a).

At this filling factor and parameter range, our results show that there is no statistically significant increase in the topological entanglement entropy as the interaction range is increased, where the integer-κ data yield $\gamma_{\kappa=1} = 0.557 \pm 0.043$, $\gamma_{\kappa=2} = 0.619 \pm 0.068$ and $\gamma_{\kappa=3} = 0.680 \pm 0.180$. Moreover, as well as agreeing with each other with a comparable precision, all of the computed γ agree with the Abelian theory prediction within standard error. Throughout this procedure, we ensure that the error standards are maintained to be $< 0.1\%$ and the linearity threshold is consistently $R^2 > 0.97$.

Note that the configurations at $n_\phi = 1/4$ and $1/5$ with $\kappa = 3$ are excluded as outliers, based on abnormal finite-size effects observed in their density profiles. Since these configurations have the smallest system sizes and MUC dimensions (4×1 and 5×1) out of the eight accepted points, it is unsurprising that they exhibit the largest finite-size effects for the case of up to third nearest-neighbor interactions.

In Fig. 4.3.(b) we present the analogous plot for the $\nu = 2/5$ state. We take the four accepted data points from Fig. 4.1.(b) and maintain the error threshold to be 0.1%. Unlike for the $\nu = 1/3$ state, at this filling factor we observe a statisti-

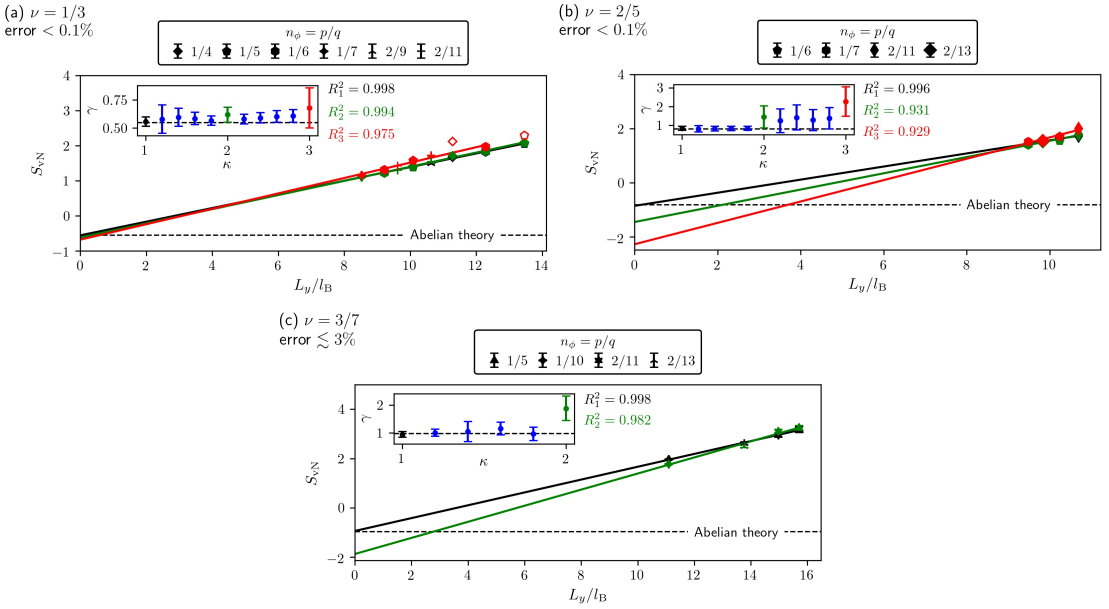

Figure 4.3.: Tuning the interaction range for the area law plots in Fig. 4.1. In each case we tune (a,b) the corresponding colored points from Fig. 4.1(a,b), and (c) the four colored points from Fig.4.1(c) that are closest to the line of best fit. The data for $\kappa = 1, 2, 3$ is colored in black, green and red, respectively, and data for intermediate values of κ is colored blue. The value of the topological entanglement entropy predicted from the Abelian theory, $\gamma = \ln(\sqrt{s})$, is additionally marked with a dashed line. In all cases, we increase the bond dimension of these runs appropriately such that we maintain the same error threshold. Consequently, the maximum bond dimension is $\chi_{\max} = 4000$ for each filling factor. The $n_\phi = 1/4$ and $1/5$, $\kappa = 3$ data points at $\nu = 1/3$ filling are marked as outliers.

cally significant increase in the topological entanglement entropy as the interaction range is increased. We find that the integer-κ data yield $\gamma_{\kappa=1} = 0.850 \pm 0.103$, $\gamma_{\kappa=2} = 1.446 \pm 0.582$, and finally $\gamma_{\kappa=3} = 2.267 \pm 0.775$.
Although this statistically significant increase hinges on a couple of data points, the mean for the $\kappa \geq 2$ data is consistently and significantly larger than both the $1 \leq \kappa < 2$ data and the Abelian theory prediction. More concretely, the topological entanglement entropies for $\kappa < 2$ confirm the Abelian nature of the state at short interaction range and have a distinctly higher precision than the $\kappa \geq 2$ data. We caution that our result at $\kappa = 3$ may be vulnerable to minor finite-size errors, particularly affecting the $n_\phi = 2/11$ data point. Although we went to great lengths

to alleviate finite-size effects at $\kappa = 1$, the quality of the configurations is expected to deteriorate as κ is increased. In order to overcome this, the same systematic procedure would have to be applied at $\kappa = 3$, which is beyong the scope of our computational resources. The errors in the data also prevent us from commenting on the continuity of the transition in the topological entanglement entropy as the interaction range is increased.
Finally, we tune the interaction range for the state at $\nu = 3/7$ filling, as shown in Fig. 4.3.(c). In this case, we take the four accepted data points that are closest to the line of best fit in Fig 4.1(c). We do this in the interests of computational expense, since the configurations for this filling are already challenging to converge, even at $\kappa = 1$. For consistency, we maintain the same error threshold. Following the observation for the $\nu = 2/5$ state, the topological entanglement entropy increases with interaction range and by a larger margin than before, from $\gamma_{\kappa=1} = 0.943 \pm 0.102$ to $\gamma_{\kappa=2} = 1.879 \pm 0.441$. The $\kappa < 2$ data solidifies the observation of an Abelian state at short interaction range and with a significantly higher precision than the result for $\kappa = 2$. We were not able to adequately alleviate numerical and statistical errors at $\kappa = 3$ for the bond dimensions that were accessible to us. However, the $\kappa = 2$ data already shows a statistically significant increase from $\kappa = 1$.

In order to verify the robustness of the FQH states at $\kappa = 1$, we examine their charge pumping and momentum-resolved entanglement spectra. In our research, we present in Fig. 4.4 the corresponding plots for the case studies introduced in Fig. 4.2. From the charge pumping curves in Fig. 4.3(a,c), we can confirm that the higher-κ states are valid FQH states corresponding to $\nu = 2/5$ and $3/7$ filling of a $|C| = 1$ band. From the $\nu = 2/5$ entanglement spectra, we notice only minor deviations in the low-lying entanglement energies, which become more pronounced as κ increases from 2 to 3. From the $\nu = 3/7$ entanglement spectra, we observe a significant deviation in the low-lying states as κ is increased, where only a small minority of the $\kappa = 1$ and 2 energies overlap. In both cases, the numerical configurations preclude a precise verification of the counting.

4.3.3. Tuning interaction strength

Having observed an increase in the topological entanglement entropy with interaction range, we now investigate the effect of increasing the interaction strength, such that $10 \leq V_0 \leq 50$, at fixed interaction range $\kappa = 1$.

In Fig. 4.5, we present the topological entanglement entropies for the $\nu = 1/3, 2/5, 3/7$ fillings, along with their associated R^2 values, as we vary V_0 for the $\kappa = 1$ configurations in Fig. 4.3. In Fig. 4.5.(a), we see that the result for $\nu = 1/3$ is stable to increases in interaction strength. In fact, the error in the

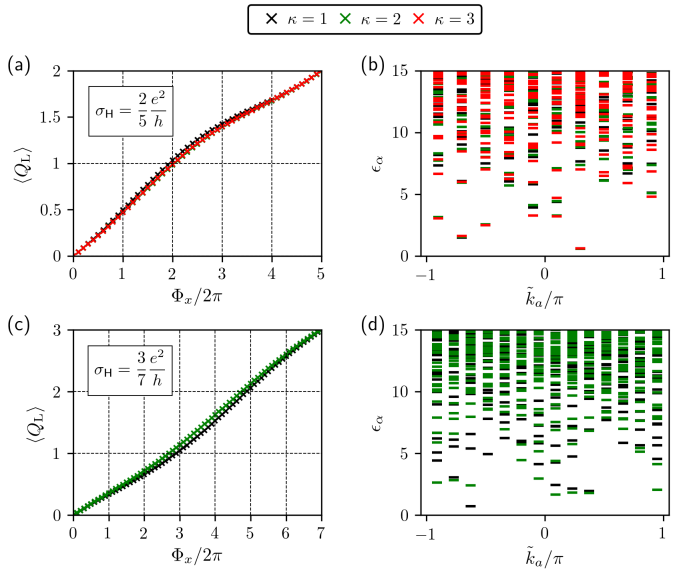

Figure 4.4.: Case studies from Fig. 4.2 as a function of κ. The results for the $\nu = 2/5$ state in (a, b) are obtained at $\chi = 800, 2000, 2000$ for $\kappa = 1, 2, 3$, respectively, whereas the results for the $\nu = 3/7$ state in (c, d) are obtained at $\chi = 2000$ for both $\kappa = 1$ and 2. These bond dimensions correspond to the values required for the area law plot in Fig. 4.3. (a, c) Average charge on the left half of the cylinder, $\langle Q_L \rangle$, as a function of the external flux, ϕ_x (See section 3.4.1). The charge pumping was performed at the reduced bond dimensions of $\chi = 400$ for $\nu = 2/5$ at $\kappa = 1$, and $\chi = 500$ for all other states. (b, d) Corresponding momentum-resolved entanglement spectra.

topological entanglement entropy decreases from $\gamma_{V_0=10} = 0.557 \pm 0.043$ to $\gamma_{V_0=50} = 0.560 \pm 0.032$ and the R^2 value monotonically increases from $R^2_{V_0=10} = 0.998$ to $R^2_{V_0=50} = 0.999$, which indicates that the result is converging, albeit slightly. In contrast, we see that in Fig. 4.5.(b), the result for $\nu = 2/5$ is not robust to increases in the interaction strength. At $V_0 = 20$ and 30, the $n_\phi = 1/6$ configuration deviates from the linear correlation, which negatively impacts the R^2 values and error bars. Moreover, at $V_0 = 40$ and 50, two of the four configurations deviate from the linear correlation, which renders an extrapolation of the topological entanglement entropy meaningless. In Fig. 4.5.(c) we observe a breakdown of the extrapolation for the $\nu = 3/7$ state already at $V_0 = 20$. In this case, the topological entanglement entropy fluctuates significantly for $V_0 \geq 20$, which is a clear indication of numerical error [86]. This analysis shows that the selected FQH configurations for the $\nu = 2/5$ and 3/7 states are prohibitively sensitive to increases in the interaction strength

in the parameter range we study. In order to successfully compute the topological entanglement entropies for these states, one would have to reevaluate the algorithm for each value of V_0, which is currently beyond the scope of our computational resources.

4.4. Discussion and conclusions

In the research presented, we investigated the Abelian topological order for the single-component $\nu = 1/3, 2/5$ and $3/7$ FQH states in the Hofstadter model with band mixing. Having developed an efficient sampling algorithm that accounts for both numerical and statistical errors, we constructed the area law of entanglement for each of these states and extrapolated to read off the topological entanglement entropies. For all states, we demonstrated topological order when interactions are nearest-neighbor. Subsequently, we investigated the effect of increasing the interaction range and strength. The non-Laughlin FQH configurations are sensitive to increases in interaction range, where we observe a corresponding increase in topological entanglement entropy, and interaction strength, to the extent that we can no longer reliably extrapolate to the thermodynamic limit. In contrast, the extrapolation for the Laughlin state is robust in both cases. These results highlight the sensitivity of Abelian FQH states in lattice models, as well as the scope of our proposed algorithm.

Given the consistent Abelian result for the topological entanglement entropy in the case of nearest-neighbor interactions, we comment briefly on the nature of these states as the interaction range and strength are increased.

In Fig. 4.3, we observe an increase in topological entanglement entropy with κ for the $\nu = 2/5$ and $3/7$ states. There are several possible explanations for this increase, including: (i) a breakdown of the FQH state, (ii) numerical error, or (iii) a transition to different quantum statistics. Scenario (i) postulates a transition from the FQH regime to a competing phase, which is conceivable, particularly in the band mixing regime [87]. However, by studying the charge pumping and entanglement spectra in Fig. 4.4, it is evident that the FQH phases have not been broken down. Scenario (ii) postulates that finite-size effects become uncontrolled as the interaction range is increased, which makes the data prohibitively noisy. Although the data is more susceptible to these effects at large κ, we place a strong emphasis on error analysis and only use the highest-quality subset of data points in Fig. 4.3. Moreover, if numerical errors were dominant, one would expect fluctuations in the topological entanglement entropy, rather than the steady increase that we observe. Scenario (iii) postulates that the Abelian FQH states transition to different quantum statistics, such as non-Abelian order [41]. With respect to the topological entanglement entropy, our data do not rule this out. Although the

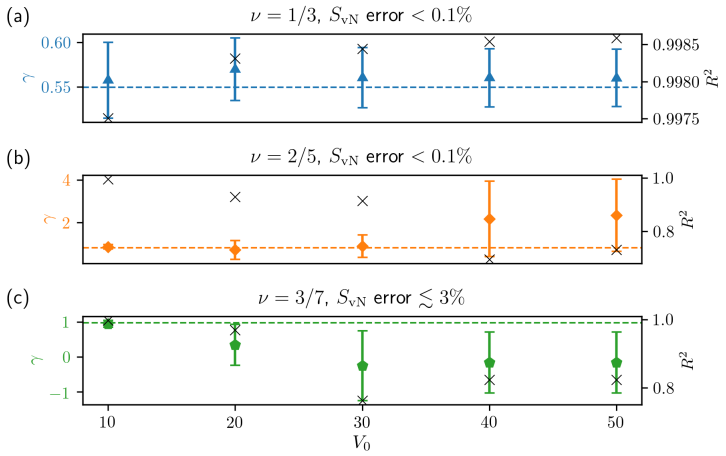

Figure 4.5.: Tuning the interaction strength for the $\kappa = 1$ area law plots in Fig. 4.3. The topological entanglement entropy data for the (a) $\nu = 1/3$, (b) $2/5$, and (c) $3/7$ series are colored blue, orange, and green, respectively. On the same axes, we plot the R^2 values of the corresponding area law plots with black crosses. The value of the topological entanglement entropy predicted from the Abelian theory, $\gamma = \ln(\sqrt{s})$, is marked with a dashed line. In all cases, the bond dimensions are the same as those for the $\kappa = 1$ plots in Fig. 4.3

$\kappa = 3$ data at $\nu = 2/5$ slightly exceeds the non-Abelian prediction of $\gamma \approx 1.448$, this may be attributed to the minor finite-size effects present for the $n_\phi = 2/11$ data point.

In Fig. 4.5, we observe that the original extrapolation of the topological entanglement entropy for the $\nu = 1/3$ state is stable to increases in interaction strength, whereas the extrapolations for the $\nu = 2/5$ and $3/7$ states are not. Indeed, the Laughlin state is known to be more robust than higher-order FQH states and has been shown numerically on a lattice to survive with interaction strengths that far exceed the band gap [17]. Moreover, we obtained a comparatively vast data set for the $\nu = 1/3$ state, which allowed us to tighten the constraints of the algorithm. As a result, the error of the entropy values for the $\nu = 1/3$ data is at least an order of magnitude smaller than the $\nu = 2/5$ state and two orders of magnitude smaller than the $3/7$ state. The finite-size effects are also reduced for the $\nu = 1/3$ state in a comparable L_y/l_B domain, which renders the topological entanglement entropy significantly more robust. For the $\nu = 2/5$ and $3/7$ states, we notice that the increased interaction strength affects the noise in our data to the extent that we can no longer reliably extrapolate to the thermodynamic limit. To accurately decouple the physical and numerical differences between the Laughlin and non-Laughlin

states and comment on the topological entanglement entropy, the algorithm would need to be reevaluated for larger values of interaction strength.

This work complements several recent investigations in both experiment and theory. In the continuum, there is a plethora of experimental phenomenology to show that the Jain series of states from $\nu = 1/3$ to $1/2$ are Abelian for the long-range Coulomb interaction [9]. In particular, the first direct experimental observation of fractional statistics was made by two independent groups last year for the $\nu = 1/3$ state, which confirms its Abelian nature [24, 25]. Moreover, theoretical investigations have been made into non-Abelian counterparts for the Jain series [88]. We note, however, that apart from the Read-Rezayi clustered states with many-body interactions [89], these states are derived from non-unitary conformal field theories, which casts doubt on whether they can describe gapped topological phases [90]. There have also been iDMRG investigations of the topological entanglement entropy of the $\nu = 2/5$ state in the continuum [78], as well as equivalent computations for trial wavefunctions directly transcribed to a MPS representation [71], which all take the Abelian value. In lattice models, there has been significant progress in experiments using optical flux lattices [91] and twisted bilayer graphene [92]. In addition, numerical investigations have found that the interaction range and strength can increase the stability of FQH states in optical lattices [93], and they have identified numerous experimental proposals to realize lattice FQH states in bilayer graphene [94, 95]. On the other hand, although the theory suggests that the statistics of elementary excitations for lattice FQH states may be sensitive to interaction range, experimental investigations in this direction for non-Laughlin lattice FQH states are still limited.

The results in our research extend this foundation in three ways. First, we investigate the $\nu = 2/5$ and $3/7$ states using iDMRG in lattice models. This is in contrast to prior research, where the topological entanglement entropy has only been investigated using iDMRG for the $\nu = 1/3$ state in lattice models [74, 75] and the $\nu = 2/5$ state in the continuum [78]. Second, in order to investigate the lattice $\nu = 2/5$ and $3/7$ states, we overcame computational and statistical challenges by developing an algorithm to construct the area law plot. Finally, we exploited this algorithm to tune the interaction range and strength, and we commented on the scope of the algorithm and nature of the states in these regimes. Finding effective ways to determine the topological order hosted by such prominent FQH plateaus is important, not only to bolster our understanding of lattice FQH states but also due to its practical implications. For example, some manifestations of the lattice FQH states discussed in our research have already been observed experimentally in bilayer graphene [80]. Moreover, advancements in optical lattices offer a promising way to tune the interaction parameters for custom lattice configurations [96].

Future studies in this area could seek to characterize the states at large κ and

V_0. Specifically, the complete anyonic statistics hae not yet been obtained from a comparable many-body simulation of the $\nu = 2/5$ and $3/7$ state in these limits. Other avenues for research include numerical simulations on the torus to confirm the incompressibility of the $\nu = 2/5$ and $3/7$ states, as well as work to establish the prerequisites for stabilizing exotic Abelian states (with $\gamma > \ln(\sqrt{s})$)). On the technical side, it would be interesting to compare our results with the approach developed by Zaletel et al., which implements the Coulomb interaction using Haldane pseudopotentials on the infinite cylinder. Coupled with this, it would be instructive to examine the effect of a dipolar interaction, to see whether the effect on topological entanglement entropy is accentuated.

We hope our research will not only emphasize the care required when constructing area laws of entanglement but, more broadly, highlight the sensitivity of Abelian lattice FQH states with respect to both interaction range and strength.

Chapter 5

Breakdown transitions of model FCIs in higher Chern bands

As we introduced in Chapter 2, FCIs generalize the FQHE states in continuum Landau levels to lattices. We also demonstrated that the Hofstadter model (see Section 2.4) is a suitable choice for stabilizing and studying FCIs, as it provides access to Chern bands of desired Chern number. In our ongoing research, our aim is to study the phase transitions where the FCI phase breaks down for this model.

A notable development comprises of numerical studies that stabilize FCIs away from the Landau-level limit, notably for higher Chern numbers $|C| > 1$ [14] and bands with a finite dispersion [15, 16]. To add to this, numerical studies also observe FCI states when the interaction energy exceeds the band gap [17, 18]. The above developments motivate the need for further investigation regarding the stability of FCI states.

We examine the entanglement energy spectrum (ES) and correlation length ξ to determine the central charge and resulting phases with respect to interaction strength and gap-to-width ratio. In this investigation we aim to examine the stability of higher Chern number FCIs, and characterize their breakdown transitions in detail. An important question towards this aim is investigating the stability in the thermodynamic limit.

The iDMRG algorithm on the infinite cylinder is again attractive for this purpose—owing to the thermodynamic limit along the x-axis, and the ease in computing the entanglement spectrum [54]. Also, as discussed in Chapter 4, iDMRG does not require band projection for the interaction Hamiltonian, and thus automatically takes band mixing into account.

5.1. Theory

Quantum phase transitions occur by tuning control parameters—we consider interaction strength and gap-to-width ratio—through a quantum critical point (QCP) in a system, and have been demonstrated for FCIs in numerical studies [31, 74].

For system configurations distant from the critical point, the entanglement en-

tropy of the ground state wavefunction is finite and the MPS ansatz is effective.

In a continuous (second order) quantum phase transition (QPT), the ground state near a critical point has long-ranged correlations, and the entanglement (quantified by the von Neumann entropy in Eq. 3.3) is expected to diverge [97]. [74] observes such a divergence in the correlation length of FCIs, and this is one indicator of a continuous phase transition. However, the MPS framework often does not allow for discerning the order, as the exact ground state near a continuous phase transition cannot be accurately represented by an MPS with finite χ—the corresponding von Neumann entropy is bounded by $\log \chi$, and the MPS state will exhibit a finite correlation length— this makes it difficult to distinguish such transitions from their first-order counterparts [98].
In order to investigate phase transitions with DMRG then, we need to figure out to what extent we can study the physics in the vicinity of the critical point with the MPS ansatz.

Computing the *central charge* c associated with the conformal field theory of the phase transition has been achieved with iDMRG, notably for FCIs in [74]. The central charge at the QCP counts the number of critical degrees of freedom and determines the finite-entanglement scaling exponent κ that relates the correlation length with χ for a continuous QPT [99].

The entanglement entropy S scales logarithmically with the correlation length ξ [100]. We refer to this as *finite entanglement scaling*—in particular, for MPS ground state wavefunctions with bond dimension χ, we expect the following relation near the critical point [99]

$$S(\chi) = \frac{c}{6} \log \xi(\chi) \tag{5.1}$$

which allows us to read off the central charge from the plot in Fig. 5.2. This entanglement scaling procedure was introduced for one-dimensional systems [99, 100], however (importantly for our research) has been applied in FCIs [74] and the continuum FQHE [101] in iDMRG studies with cylinder geometries—where the authors vary χ to obtain multiple points in the S vs. $\log \xi$ plot. However, we can obtain such a plot also by taking the multiple points for a constant χ near the critical point as in Fig. 5.2.

The applicability of this entanglement scaling procedure in [74] is further discussed in [98]—it is argued based on the observation that the finite MPS correlation length ξ near a QCP is much larger than the cylinder circumference L_y for a large enough χ. This implies the entanglement of degrees of freedom far away from our cut, and allows one to use the 1D critical scaling [98].

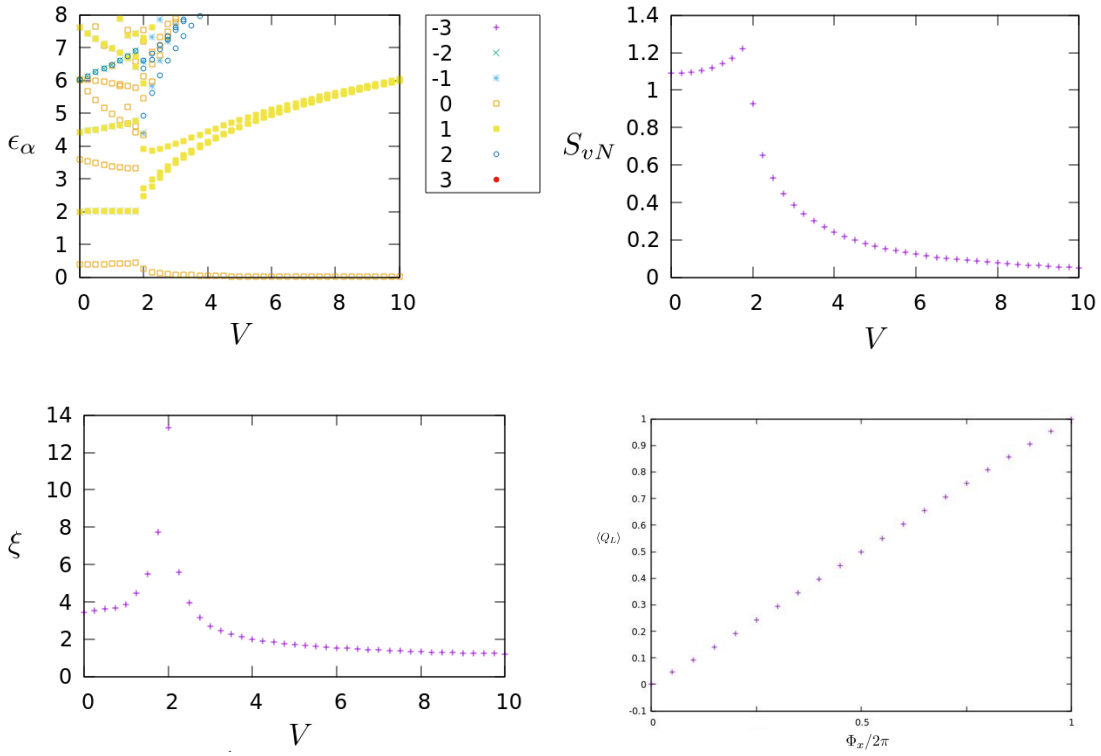

Figure 5.1.: Case study for a CI-to-metal breakdown transition in the Haldane model, with respect to interaction strength. Data has been computed at a bond dimension $\chi = 200$. We plot the [(a)] entanglement energies ϵ_α, [(b)] entanglement entropy S_{vN} and [(c)] correlation length computed as a function of interaction strength V. [(d)] Charge pumping computed in the CI regime. Insertion of one flux into the cylinder leads to one charge pumped, and thus $\sigma_H \sim e^2/h$, verifying the $C = 1$ CI nature of the ground state.

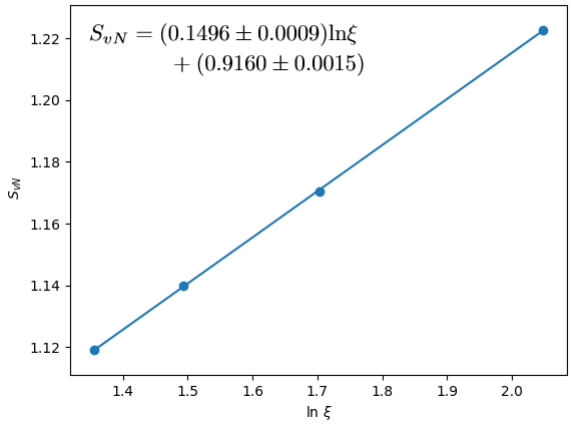

Figure 5.2.: We compute the central charge c from Eq. 5.1 for the case study discussed in Section 5.2 and Fig. 5.1. In particular, we considered points $(\ln \xi, S_{vN})$ in the vicinity of the phase transition. The central charge is associated with the conformal field theory of the phase transition [74]. We obtain $c = 0.898 \pm 0.0054$.

5.2. Case study 1: CI-to-metal transition

As a starting point, we consider a CI-to-metal transition (see Fig. 5.1) for the Haldane model [102]. As such transitions have been well studied, this provides a verification for our numerics and allows us motivate our methods through example. In particular we study the ES, correlation length and entanglement entropy with respect to the interaction strength. The ES clearly resolves the two distinct phases, with the transition occuring at $V = 2$. The phase at $V < 2$ consists of a dense ES for the CI. We recall that characterizing the order of the phase transition is a task that the MPS framework is not ideal for, as the ansatz always has a finite entanglement.
Clear signatures of the phase transition are observed in the correlation length ξ, which peaks at the QCP, followed by a significant drop in in the metallic regime. Further, we can compute the central charge from Fig. 5.2, where the four points on the plot are taken near the critical point in the metallic phase—See Fig. 5.2.

5.3. Current status of research

Our research is ongoing—the first step (and challenge) involves stabilizing the FCIs on various configurations of the Hofstadter model that yield desired Chern numbers. This involves running computations for several parameters, such as

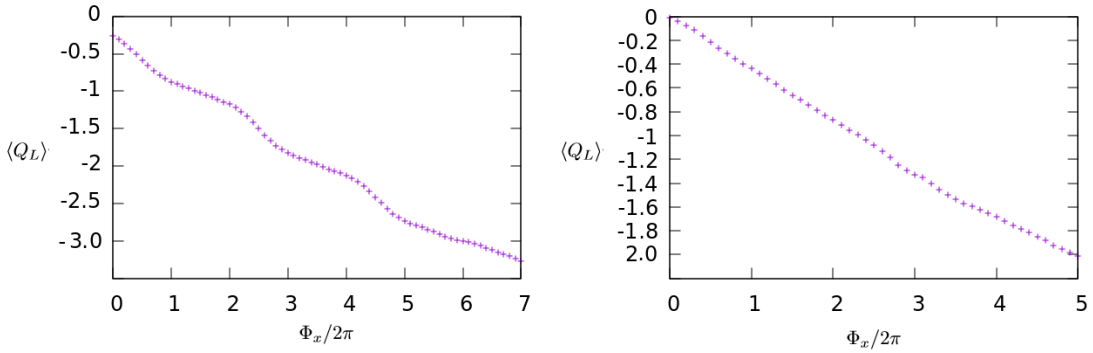

a $\nu = 1/5, C = 2$ b $\nu) = 1/7, C = 3$

Figure 5.3.: We utilize the charge pumping to verify the FCI nature of our states. The Hall conductivity for a FCI with Chern number C is given as $\sigma_H = (e^2/h)C\nu$, where $\nu(= p/q)$ is the filling factor of the system. This corresponds to Cp charges pumped in q flux insertions, which we confirm here for two higher Chern number states.

circumference L_y (an optimal length must be considered that mitigates finite-size effects but is also computationally feasible), bond dimension χ and flux densities n_ϕ. We have identified that for our investigation, it is further important to study the dependence of our FCI states on these parameters.
Once we stabilize these FCIs, we can tune the control parameters and search for breakdown transitions.
Currently, we have stabilized various FCIs with higher Chern numbers in the Hofstadter model—further the FCI nature of these states has been verified through charge pumping (Fig. 5.3 provides this for FCIs with $C = 2$ and 3). We are also investigating our numerical evidence that suggests a $C = 5$ FCI.
The features of a metal-to-FCI transition that we observed in the Hofstadter model are presented in Fig. 5.4. In particular, we consider the Laughlin filling fraction $\nu = 1/3$, with the cylinder circumference $L_y = 6$ and $\chi = 250$.
We state that the project is still a work in progress—our aim in this section was to motivate this research and provide an account of the current status.

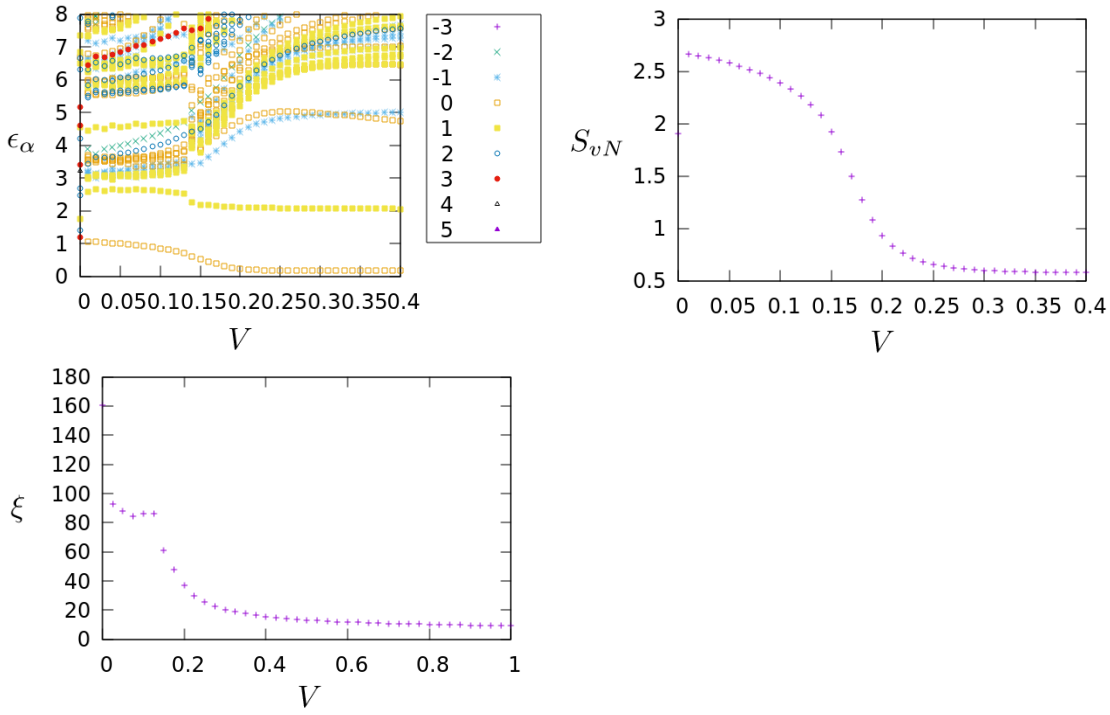

Figure 5.4.: Observed metal-to-FCI breakdown transition in the Hofstadter model with respect to interaction strength. Data has been computed at a bond dimension $\chi = 250$. Clear signs of phase transitions are observed in the [(a)] entanglement energies ϵ_α, [(b)] entanglement entropy S_{vN} and [(c)] correlation length vs. V plots. Computing the central charge for this transition would require an increase in χ.

Chapter 6

Conclusion

In this thesis, we have investigated FQHE states on a lattice. Numerical studies of FCIs are important to characterize the topological order, and can shed light on their stability. These studies have also led to various interesting observations that motivate the need for further investigation, such as lattice-specific states [14] and stability of states away from the Landau-level limit [17, 18]. Through our research, we aimed to illuminate the nature of these FCIs, and answer some fundamental questions about their topological order and stability. We have also contributed to the field of numerical investigation of FCIs, by devising a systematic and efficient method towards characterizing topological order of model FCIs, and observed—in the main result of this thesis— Abelian topological order for nearest-neighbor interactions in the $\nu = 2/5$ and $3/7$ states.

Let us recap what we have covered and achieved in this thesis.
We started off by introducing the theory of the FQHE, motivated the need to study the excitations of the ground state, and introduced the concepts of fractional charge and statistics. We also studied the Hofstadter model and plotted the single-particle spectrum. We argued how we can tune the parameters of the model to stabilize FCIs, notably for higher Chern numbers.

We then discussed the Matrix Product State (MPS) formalism, its effectiveness and its shortcomings, especially in two dimensions. We introduced the DMRG algorithm and described its implementation as a variational method in the MPS framework. We presented various techniques that we used in our research to characterize FCI states and to confirm their FQH nature.

Then we moved on to the main research of our thesis—the investigation of topological order for $\nu = 2/5$ and $3/7$ FQH states on a lattice. We used the iDMRG algorithm on an infinite cylinder geometry to compute ground states and corresponding area law plots. We exploit this area law scaling for two dimensions to obtain the topological entanglement entropy. We developed an efficient algorithm for this computation, which allowed us to probe the topological order of these states. We identified Abelian order for the filling factors of interest for nearest-neighbor interactions. We also investigated the sensitivity of this routine with respect to the interaction range and observed an increase in the topological entanglement entropy, for which we discussed the different possible explanations.

Finally, we introduced our current research on the stability of FCIs with a higher Chern number. We described the numerical tools used to study and characterize the breakdown transitions of FCIs. We presented our current work towards this goal, which has involved stabilizing FCIs for various configurations of the Hofstadter model.

Appendix A

Numerical method

In an effort to remove arbitrariness from the computation of topological entanglement entropies, we follow a set algorithm for the data collection and analysis. In this appendix, we outline and justify the steps in the procedure. We start with a description of the systematic selection of n_ϕ values in Sec. A.1, we then explain how the entanglement entropy is extrapolated for each configuration in Sec. A.2, and finally show how the line of best fit is constructed for the area law of entanglement in Sec. A.3.

A.1. Selection of n_ϕ

For a given filling factor, we list all values of the coprime fraction $n_\phi \equiv p/q$ that satisfy the following constraints:

- $\frac{1}{2\pi}\left(\frac{(L_y/l_B)_{\min}}{L_y}\right)^2 < n_\phi < 0.4$

  Due to finite-size effects, we can safely set a lower bound on the $L_y/l_B = \sqrt{2\pi n_\phi} L_y$ values that we produce. From preliminary investigations of the bosonic Laughlin state [Fig. B.1.(a)], the simplest FQH state, we found that finite-size effects are sufficiently suppressed at $L_y/l_B \gtrsim 8$. Since finite-size effects for higher-order FQH states require larger cylinder circumferences to be suppressed, we set at least $(L_y/l_B)_{\min} \equiv 8$. As we proceed up the FQH hierarchy, we can increase this minimum threshold. Furthermore, it has been shown experimentally that Laughlin states require $n_\phi < 0.4$ to be stabilized and that this critical n_ϕ may be lower for higher-order hierarchy states [93]. Hence, we set the upper limit for the flux densities to 0.4.

- $L_y \geq 4$

  Since we are interested in the effect of tuning the interaction range across first, second, and third nearest neighbors, we demand that the system size is at least four sites across in the y-direction.

- $4 \leq q \leq 20$

Similar to above, we demand that the system size in the x-direction is also at least four sites across[i]. Furthermore, we set the maximum value to 20 so that we limit the precision of the required flux density values. This makes the results more relevant for experimental set-ups, such as optical flux lattices [103].

- $N_{\min} \geq 2$

  We require that the total number of particles in our system ($N = nqL_xL_y$) is an integer greater than or equal to two, for two-body interactions.

- $qL_xL_y \leq N_{\mathrm{s,max}}$

  We limit the total size of the MPS unit cell to be less than or equal to $N_{\mathrm{s,max}}$. This restricts the memory cost, which scales linearly with the system size. We adjust the value $N_{\mathrm{s,max}} \sim 100$ depending on computational resources.

- $\Delta_{L_y/l_B} > 0.1$

  We require that the separation between L_y/l_B values is greater than 0.1. This is to minimize the susceptibility of the line of best fit to errors in the individual values for the entanglement entropies. It also efficiently provides a greater range of L_y/l_B values to consider. The value of 0.1 was chosen as a compromise between precision and a maximal data set.

Finally, we define a processing cost function $\Gamma(p, q, L_x, L_y) \equiv qL_x\mathrm{e}^{L_y+\tilde{n}_\phi}$, where $\tilde{n}_\phi = 20n_\phi$ is the normalized flux density, defined such that the range $1 \leq \tilde{n}_\phi < 8$ is comparable to $6 \lesssim L_y \lesssim 15$. We then sort the configurations in ascending Γ, attempt to converge all of them up to $\chi_{\max} \lesssim 3000$, and use those that are successful.

The processing cost function roughly quantifies how much processing time is needed for a state to converge. It is not the physical processing cost of the iDMRG algorithm itself, which scales (conservatively) as $\sim O(\chi^3 Dd^3 + \chi^2 D^2 d^2)$ for a single bond update, where D is the MPO bond dimension and d is the single-site Hilbert space dimension. Rather, the processing cost function takes into account the χ required for convergence in a given model. It is well known that the convergence processing cost of the iDMRG algorithm scales linearly with cylinder length and exponentially with cylinder circumference. Moreover, from preliminary investigations of the Laughlin states, we find that a state is more likely to converge with a smaller n_ϕ, showing roughly the same scaling precedence as cylinder circumference.

[i] These conditions on L_y and q do not guarantee that a system will be large enough to sufficiently suppress finite-size effects, as exemplified by the outlier in Fig. 4.3.(a).

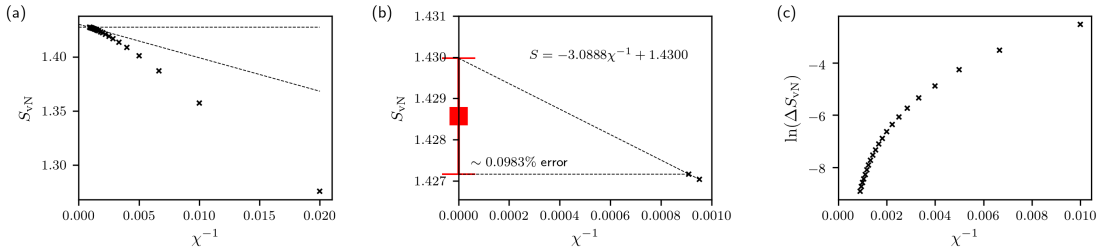

Figure A.1.: Extrapolation of the entanglement entropy, S_{vN}, in the $\chi \to \infty$ limit for the fermionic Hofstadter model at $\nu = 1/3$, with flux density $n_\phi = 1/3$ and cylinder circumference $L_y = 6$. (a) S_{vN} as a function of χ^{-1}, where $\chi \in [50, 100, 150, \ldots, 1100]$. (b) A close-up of the last two points shown in (a), including the equation of the straight line through these points, and the $\lim_{\chi\to\infty}(S_{\mathrm{vN}})$ estimate with error bars shown in red. (c) The change in entropy as the bond dimension is incremented, ΔS_{vN}, for the data points in (a).

A.2. Extrapolation of the entanglement entropy to the $\chi \to \infty$ limit

Since the final result for the topological entanglement entropy, γ, is highly sensitive to the values of the individual entanglement entropies, S_{vN}, we need to minimize the error in S_{vN} to obtain a representative value for γ. Furthermore, since we are comparing γ between different Hamiltonians, we additionally need to ensure that all S_{vN} are computed to the same accuracy for a fair comparison.

To this end, we study the convergence of S_{vN} with bond dimension χ. An illustrative example for the Laughlin state in the fermionic Hofstadter model is shown in Fig. A.1. Figures A.1.(a,b) show the convergence of S_{vN} with χ for this system. We can see that as χ is increased, the entropy is approaching a value of 1.43. To quantify this, we note that entropy increases monotonically with bond dimension, as demonstrated in Fig. A.1.(c). Hence, the highest-χ value for S_{vN} will be the lower bound of our entropy estimate. Moreover, we know that in the $\chi \to \infty$ limit, $\mathrm{d}S_{\mathrm{vN}}/\mathrm{d}\chi \to 0$, which implies that $\mathrm{d}S_{\mathrm{vN}}/\mathrm{d}\chi$ monotonically decreases. Hence the extrapolation of our last estimate of $\Delta S_{\mathrm{vN}}/\Delta\chi$ will serve as our upper bound. Since a polynomial fit of all data points is computationally costly, and will have negligible benefits as we reduce the errors, we instead take $\lim_{\chi\to\infty} S_{\mathrm{vN}}$ to be directly in between our lower and upper bounds, as exemplified by the red data point in Fig. A.1.(b).

In order to maintain a consistent accuracy among all entanglement entropy values in this manuscript, we continue with the entropy convergence until all

$\lim_{\chi\to\infty} S_{\mathrm{vN}}$ estimates have error bars $< 0.1\%$, unless otherwise stated. Consequently, the example system in Fig. A.1 is sufficiently converged for $\chi_{\max} = 1100$.

A.3. Linear regression

For a given area law plot of the entanglement entropy, there can be great variability in the y-intercept of the linear regression depending on which points are considered, as shown in Fig. B.1. Moreover, it is known that finite-size effects become significant for small systems, and in the extreme case, the area law even breaks down since $S = \alpha L_y - \gamma + O(\mathrm{e}^{-L_y})$. Therefore, there is motivation to carefully reject data with small cylinder circumferences without biasing the final result for the topological entanglement entropy. To reconcile this issue, we use an algorithm to construct the line of best fit.

For all the data points on the plot, we draw lines of best fit: the first of which considers all of the data, the second rejects the smallest L_y/l_B point, the third rejects the smallest two L_y/l_B points, etc. We continue in this manner until we reach a line that satisfies $R^2 > 0.99$. It is this line that we use for our linear regression. The data is quantifiably linear and so finite-size effects are suppressed, and we take the first such line because it is based on the most points.

Appendix B

Complete data sets

In Fig. B.1, we present the complete set of data collected in this project for $\kappa = 1$, both systematic and unsystematic. Along with the area law of entanglement in the top panel of each plot, we also present the topological entanglement entropy estimate from including all points with a cylinder circumference $\geq L_y/l_B$ (middle panel), along with the corresponding R^2 values for each of these linear regressions (bottom panel).

In Fig. B.1.(a,b) we show data for the bosonic and fermionic Laughlin states. For the bosonic Laughlin state, we computed the entanglement entropy for 76 configurations, 46 of which converged with $< 0.1\%$ error and are shown in Fig. B.1.(a). Even with the complete $< 0.1\%$ error data set, we still obtain a clear agreement with the Abelian theory value of $\gamma = \ln(\sqrt{2}) \approx 0.347$. We also note that after the $R^2 = 0.99$ threshold, finite-size effects are suppressed since we maintain $R^2 > 0.99$, and the average topological entanglement entropy agrees with the theory based on all values drawn after this point. This plot also highlights the dramatic effect that a few relatively minor outliers (notably $\{n_\phi = 1/3,\ L_y = 4\}$ and $\{n_\phi = 2/7,\ L_y = 6\}$) can have on the topological entanglement entropy estimate and raises concerns of selection bias in unsystematic studies. For the fermionic Laughlin state, we computed the entanglement entropy for 89 configurations, 53 of which converged and are shown in Fig. B.1.(b). Overall, we notice similar features as for the bosonic Laughlin state. However, we note that on this occasion the complete $< 0.1\%$ error data set does not agree with the Abelian theory. We emphasize that, as with the bosonic Laughlin state, it is simply coincidence whether or not the complete data set agrees with the theory due to the significant finite-size effects at small cylinder circumference. Once we draw a line through all points above the $R^2 = 0.99$ threshold, we do see a clear agreement. As with the bosonic Laughlin state, $R^2 > 0.99$ is maintained above this threshold, which indicates that finite-size effects have been effectively alleviated. Note also that the $R^2 > 0.99$ threshold occurs at $L_y/l_B = 9.21$, which is larger than the bosonic value $L_y/l_B = 8.12$, as expected.

Motivated by the results from the Laughlin states, we construct corresponding plots for the next filling factors in the hierarchy: the bosonic $\nu = 2/3$ and fermionic $\nu = 2/5$ states, shown in Fig. B.1.(c–e). For the bosonic $\nu = 2/3$ state,

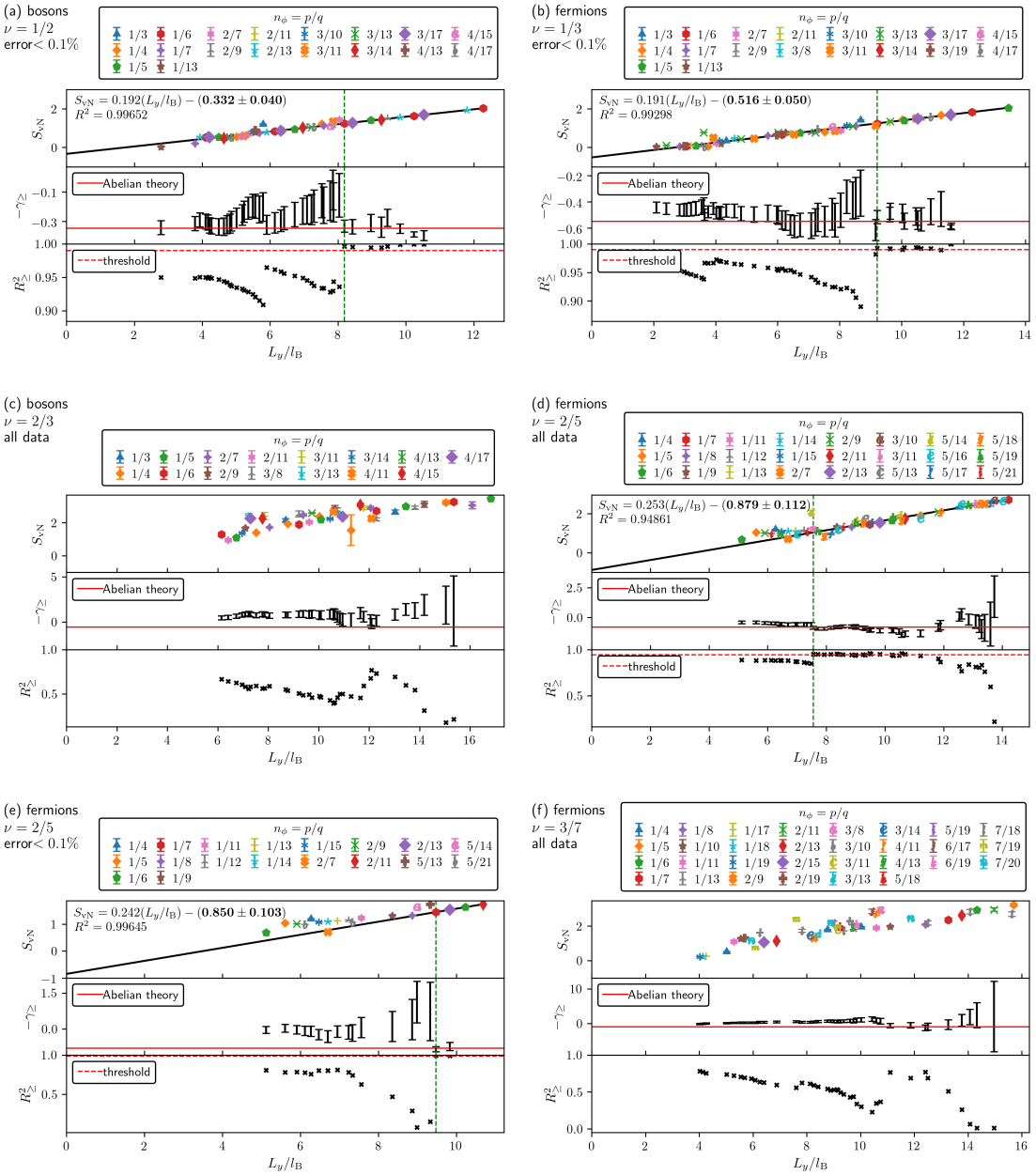

Figure B.1.: The complete data sets for the: (a) bosonic and (b) fermionic Laughlin (0th hierarchy) states with $< 0.1\%$ error; the (c) complete bosonic, (d) complete fermionic, and (e) $< 0.1\%$ error fermionic 1st hierarchy states; and (f) the fermionic 2nd hierarchy state. (top panels) Von Neumann entanglement entropy, S_{vN}, plotted as a function of cylinder circumference, L_y, in units of magnetic length, $l_B = (2\pi n_\phi)^{-1/2}$. The line of best fit is drawn through the set of points above the smallest L_y/l_B that yields $R^2 > 0.99$ for $< 0.1\%$ error data and $R^2 = R^2_{\text{max}}$ otherwise. This cut-off is marked with a green dashed line. (middle panels) The y-intercept of the line of best fit drawn through all points greater than or equal to L_y/l_B, denoted as $-\gamma_\geq$. The Abelian theory prediction, $\gamma = \ln(\sqrt{s})$, is marked in red. (bottom panels) The square of Pearson's correlation coefficient for the line of best fit drawn through all points greater than of equal to L_y/l_B, denoted as $R^2_\geq$. The corresponding threshold, either $R^2 = 0.99$ or R^2_{max}, is marked with a red dashed line.

we computed the entanglement entropy for 41 configurations, only 5 of which converged, and so we simply show all of the data in Fig. B.1.(c). For this filling factor, we are not able to draw any conclusions regarding the topological entanglement entropy. We note incidentally, however, that the value of the topological entanglement entropy for the largest R^2 value gives the closest agreement with the Abelian theory, which indicates potential agreement once finite-size effects are alleviated. For the fermionic $\nu = 2/5$ state we computed 50 entanglement entropies, shown in Fig. B.1.(d), and 20 converged to $< 0.1\%$ error, shown in Fig. B.1.(e). In this case, when a line is drawn through *all* data points above the R^2_{max} threshold in Fig. B.1.(d), we obtain a close agreement to the Abelian theory value, similar to the result obtained using the $< 0.1\%$ error data. We note however, that the R^2 value does not maintain its large value after the threshold, which indicates that significant fluctuations are still present. In contrast, when we examine exclusively $< 0.1\%$ error data points in Fig. B.1.(e), we see that $R^2 > 0.99$ is maintained after the threshold. In keeping with the noted trend, the value at which this occurs, $L_y/l_B = 9.47$, is higher than for the corresponding Laughlin state.

Most ambitiously, we construct an area law plot for the secondary fermionic hierarchy state at $\nu = 3/7$. For this state, we computed the entanglement entropy for 44 configurations, only 12 of which converged to $< 0.1\%$ error. Consequently, we present all of the data in Fig. B.1.(f). Given the immense computational effort in obtaining high-L_y/l_B data for the $\nu = 3/7$ state ($\sim$ 256GB of memory and ~ 2 weeks run-time per data point), we analyze this as a stand-alone plot. As demonstrated in Fig. B.1.(d), we cannot reliably apply the R^2 threshold analysis, since the error of the data set is not small enough. We also note that for this system both physical (L_y/l_B) and numerical (L_y) finite-size effects are significant. Taking the largest system sizes that we considered, with respect to both length scales, yields the subset shown in Fig. 4.1.(c). The extracted data is still significantly noisier than any other data presented in the main text, however the complete data set suggests that these finite-size effects will be alleviated if the cylinder circumference is further increased. Specifically, we again point out that the estimate of the topological entanglement entropy with the largest R^2 value yields the closest agreement to the Abelian theory. This is true for all of the area law plots in our analysis.

Appendix C

Total quantum dimensions

Generalized parafermion FQH states are expected at the filling $\nu = k/(Mk+2)$, where M even/odd corresponds to bosons/fermions and k is an integer [89]. These states are described by a $SU(2)_k$ Chern-Simons theory in the bulk and the rational CFT $[SU(2)/U(1)]_k \times U(1)_{k(MK+2)}$ on the edge [79]. Since the total quantum dimensions for $SU(2)$ or $U(1)$ theories with positive and negative k levels are identical, the total quantum dimension for the coset theory is given as

$$\mathcal{D}_{\text{coset}} = \frac{\sqrt{(|k|+2)|Mk+2|}}{2\sin\left(\frac{\pi}{|k|+2}\right)}. \tag{C.1}$$

For the non-Abelian $\nu = 2/5$ state we may set $k = 3$, $M = 1$ to yield $\mathcal{D}_{2/5} = \sqrt{5(\varphi^2+1)}$, whereas for the non-Abelian $\nu = 3/7$ state we may set $k = -3$, $M = 3$ to yield $\mathcal{D}_{3/7} = \sqrt{7(\varphi^2+1)}$. Note that in both cases this is larger than the minimum Abelian value for the total quantum dimension $\sqrt{s}$ by a factor of $\sqrt{\varphi^2+1}$.

Since both the $\nu = 2/5$ and $3/7$ non-Abelian theories have $|k| = 3$, they describe a theory of Fibonacci anyons [104]. As mentioned in the main text, the total quantum dimension must take the form $\mathcal{D} = \sqrt{\sum_a d_a^2}$, where d_a is the quantum dimension of a quasiparticle of type a. For Abelian anyons $d_a = 1$, whereas for non-Abelian anyons $d_a > 1$ [44]. Furthermore, for any $\nu = r/s$ FQH state the ground-state degeneracy must be at least s, which confirms the minimum Abelian value for the total quantum dimension $\sqrt{s}$. In addition to Abelian anyons, a Fibonacci theory also hosts non-Abelian anyons of quantum dimension φ [105]. Therefore, based on these two arguments alone, the total quantum dimension for a $|k| = 3$ theory must take the form $\mathcal{D}_{|k|=3} = \sqrt{\alpha\varphi^2+\beta}$, where α, β are positive integers satisfying $\alpha + \beta \geq s$.

Bibliography

[1] Bartholomew Andrews, Madhav Mohan, and Titus Neupert. Abelian topological order of $\nu = 2/5$ and $3/7$ fractional quantum hall states in lattice models. *Physical Review B*, 103(7):075132, February 2021.

[2] Johannes Hauschild and Frank Pollmann. Efficient numerical simulations with Tensor Networks: Tensor Network Python (TeNPy). *SciPost Physics Lecture Notes*.

[3] GNU Parallel 20150322 ('Hellwig'), March 2015.

[4] The Nobel Prize in Physics 2016, https://www.nobelprize.org/prizes/physics/2016/summary/.

[5] K. v. Klitzing, G. Dorda, and M. Pepper. New Method for High-Accuracy Determination of the Fine-Structure Constant Based on Quantized Hall Resistance. *Physical Review Letters*, 45(6):494–497, August 1980.

[6] D. C. Tsui, H. L. Stormer, and A. C. Gossard. Two-Dimensional Magnetotransport in the Extreme Quantum Limit. *Physical Review Letters*, 48(22):1559–1562, May 1982.

[7] D. J. Thouless, M. Kohmoto, M. P. Nightingale, and M. den Nijs. Quantized Hall Conductance in a Two-Dimensional Periodic Potential. *Physical Review Letters*, 49(6):405–408, August 1982.

[8] R. B. Laughlin. Anomalous Quantum Hall Effect: An Incompressible Quantum Fluid with Fractionally Charged Excitations. *Physical Review Letters*, 50(18):1395–1398, May 1983.

[9] Jainendra K. Jain. *Composite Fermions*. Cambridge University Press, Cambridge, 2007.

[10] N. Regnault and B. Andrei Bernevig. Fractional Chern Insulator. *Physical Review X*, 1(2):021014, December 2011. arXiv: 1105.4867.

[11] Thomas Scaffidi and Gunnar Möller. Adiabatic Continuation of Fractional Chern Insulators to Fractional Quantum Hall States. *Physical Review Letters*, 109(24):246805, December 2012.

[12] Ying-Hai Wu, J. K. Jain, and Kai Sun. Adiabatic continuity between Hofstadter and Chern insulator states. *Physical Review B*, 86(16):165129, October 2012.

[13] Chetan Nayak, Steven H. Simon, Ady Stern, Michael Freedman, and Sankar Das Sarma. Non-Abelian anyons and topological quantum computation. *Reviews of Modern Physics*, 80(3):1083–1159, September 2008.

[14] Gunnar Möller and Nigel R. Cooper. Fractional Chern Insulators in Harper-Hofstadter Bands with Higher Chern Number. *Physical Review Letters*, 115(12):126401, September 2015.

[15] A. M. Läuchli, Zhao Liu, E. J. Bergholtz, and R. Moessner. Hierarchy of Fractional Chern Insulators and Competing Compressible States. *Physical Review Letters*, 111(12):126802, September 2013.

[16] Adolfo G. Grushin, Titus Neupert, Claudio Chamon, and Christopher Mudry. Enhancing the stability of a fractional Chern insulator against competing phases. *Physical Review B*, 86(20):205125, November 2012.

[17] Stefanos Kourtis, Titus Neupert, Claudio Chamon, and Christopher Mudry. Fractional Chern Insulators with Strong Interactions that Far Exceed Band Gaps. *Physical Review Letters*, 112(12):126806, March 2014.

[18] D. N. Sheng, Zheng-Cheng Gu, Kai Sun, and L. Sheng. Fractional quantum Hall effect in the absence of Landau levels. *Nature Communications*, 2(1):389, July 2011.

[19] Richard E. Prange and Steven M. Girvin, editors. *The Quantum Hall Effect*. Maryland Subseries: Based on Lectures at the University of Maryland, College Park. Springer-Verlag, New York, 2 edition, 1990.

[20] A. H. MacDonald. Introduction to the Physics of the Quantum Hall Regime. *arXiv:cond-mat/9410047*, October 1994. arXiv: cond-mat/9410047.

[21] David Tong. Lectures on the Quantum Hall Effect. *arXiv:1606.06687 [cond-mat, physics:hep-th]*, September 2016. arXiv: 1606.06687.

[22] Jörg Behrmann, Zhao Liu, and Emil J. Bergholtz. Model Fractional Chern Insulators. *Physical Review Letters*, 116(21):216802, May 2016. arXiv: 1512.04553.

[23] R. de Picciotto, M. Reznikov, M. Heiblum, V. Umansky, G. Bunin, and D. Mahalu. Direct Observation of a Fractional Charge. *Physica B: Condensed Matter*, 249-251:395–400, June 1998. arXiv: cond-mat/9707289.

[24] J. Nakamura, S. Liang, G. C. Gardner, and M. J. Manfra. Direct observation of anyonic braiding statistics. *Nature Physics*, 16(9):931–936, September 2020.

[25] H. Bartolomei, M. Kumar, R. Bisognin, A. Marguerite, J.-M. Berroir, E. Bocquillon, B. Plaçais, A. Cavanna, Q. Dong, U. Gennser, Y. Jin, and G. Fève. Fractional statistics in anyon collisions. *Science*, 368(6487):173–177, April 2020.

[26] Daniel Arovas, J. R. Schrieffer, and Frank Wilczek. Fractional Statistics and the Quantum Hall Effect. *Physical Review Letters*, 53(7):722–723, August 1984.

[27] Sumathi Rao. Introduction to abelian and non-abelian anyons. In *Topology and Condensed Matter Physics*, Texts and Readings in Physical Sciences, pages 399–437. Springer, Singapore, 2017.

[28] X. G. Wen. Topological orders in rigid states. *International Journal of Modern Physics B*, 04(02):239–271, February 1990.

[29] B.A. Bernevig and T.L. Hughes. *Topological Insulators and Topological Superconductors*. April 2013.

[30] Fenner Harper. *The Hofstadter model and other fractional chern insulators*. Phd thesis, University of Oxford, 2015.

[31] Adolfo G. Grushin, Johannes Motruk, Michael P. Zaletel, and Frank Pollmann. Characterization and stability of a fermionic ν=1/3 fractional chern insulator. *Physical Review B*, 91(3):035136, January 2015. arXiv: 1407.6985.

[32] Y. Aharonov and D. Bohm. Significance of Electromagnetic Potentials in the Quantum Theory. *Physical Review*, 115(3):485–491, August 1959.

[33] R. Peierls. Zur Theorie des Diamagnetismus von Leitungselektronen. *Zeitschrift für Physik*, 80(11):763–791, November 1933.

[34] Douglas R. Hofstadter. Energy levels and wave functions of Bloch electrons in rational and irrational magnetic fields. *Physical Review B*, 14(6):2239–2249, September 1976.

[35] Felix Bloch. Über die Quantenmechanik der Elektronen in Kristallgittern. *Zeitschrift für Physik*, 52(7):555–600, July 1929.

[36] Monika Aidelsburger. *Artificial gauge fields with ultracold atoms in optical lattices*. Phd thesis, Ludwig-Maximilians-Universität München, February 2015.

[37] J. Zak. Magnetic Translation Group. *Physical Review*, 134(6A):A1602–A1606, June 1964.

[38] J. Zak. Proper Functions for a Bloch Electron in a Magnetic Field. *Physical Review*, 139(4A):A1159–A1162, August 1965.

[39] Bartholomew Andrews and Gunnar Möller. Stability of fractional Chern insulators in the effective continuum limit of Harper-Hofstadter bands with Chern number $|C| > 1$. *Physical Review B*, 97(3):035159, January 2018.

[40] Zhao Liu, D. L. Kovrizhin, and Emil J. Bergholtz. Bulk-edge correspondence in fractional Chern insulators. *Physical Review B*, 88(8):081106, August 2013.

[41] Zhao Liu, Emil J. Bergholtz, and Eliot Kapit. Non-Abelian fractional Chern insulators from long-range interactions. *Physical Review B*, 88(20):205101, November 2013.

[42] Bartosz Kuśmierz and Arkadiusz Wójs. Emergence of Jack ground states from two-body pseudopotentials in fractional quantum Hall systems. *Physical Review B*, 97(24):245125, June 2018.

[43] Nicolas Laflorencie. Quantum entanglement in condensed matter systems. *Physics Reports*, 646:1–59, August 2016. arXiv: 1512.03388.

[44] Alexei Kitaev and John Preskill. Topological Entanglement Entropy. *Physical Review Letters*, 96(11):110404, March 2006.

[45] Don N. Page. Average entropy of a subsystem. *Physical Review Letters*, 71(9):1291–1294, August 1993.

[46] J. Eisert, M. Cramer, and M. B. Plenio. Colloquium: Area laws for the entanglement entropy. *Reviews of Modern Physics*, 82(1):277–306, February 2010.

[47] U. Schollwöck. The density-matrix renormalization group. *Reviews of Modern Physics*, 77(1):259–315, April 2005.

[48] Stefan Rommer and Stellan Östlund. Class of ansatz wave functions for one-dimensional spin systems and their relation to the density matrix renormalization group. *Physical Review B*, 55(4):2164–2181, January 1997.

[49] Ian Affleck, Tom Kennedy, Elliott H. Lieb, and Hal Tasaki. Rigorous results on valence-bond ground states in antiferromagnets. *Physical Review Letters*, 59(7):799–802, August 1987.

[50] Johannes Motruk, Michael P. Zaletel, Roger S. K. Mong, and Frank Pollmann. Density matrix renormalization group on a cylinder in mixed real and momentum space. *Physical Review B*, 93(15):155139, April 2016. arXiv: 1512.03318.

[51] Steven R. White. Density matrix formulation for quantum renormalization groups. *Physical Review Letters*, 69(19):2863–2866, November 1992.

[52] Ulrich Schollwoeck. The density-matrix renormalization group in the age of matrix product states. *Annals of Physics*, 326(1):96–192, January 2011. arXiv: 1008.3477.

[53] Lukasz Cincio and Guifre Vidal. Characterizing topological order by studying the ground states of an infinite cylinder. *arXiv:1208.2623 [cond-mat, physics:quant-ph]*, August 2012. arXiv: 1208.2623.

[54] Hui Li and F. D. M. Haldane. Entanglement Spectrum as a Generalization of Entanglement Entropy: Identification of Topological Order in Non-Abelian Fractional Quantum Hall Effect States. *Physical Review Letters*, 101(1):010504, July 2008.

[55] L. Cincio and G. Vidal. Characterizing Topological Order by Studying the Ground States on an Infinite Cylinder. *Physical Review Letters*, 110(6):067208, February 2013.

[56] T. Chakraborty and P. Pietilainen. *The quantum Hall effects: integral and fractional*. Number 85 in Springer series in solid-state sciences. Springer-Verlag, Berlin ; New York, 2nd enl. and updated ed edition, 1995.

[57] Songyang Pu, Ying-Hai Wu, and J. K. Jain. Composite Fermions on a Torus. *Physical Review B*, 96(19):195302, November 2017. arXiv: 1708.08816.

[58] J. M. Leinaas and J. Myrheim. On the theory of identical particles. *Il Nuovo Cimento B (1971-1996)*, 37(1):1–23, January 1977.

[59] Frank Wilczek. Quantum Mechanics of Fractional-Spin Particles. *Physical Review Letters*, 49(14):957–959, October 1982.

[60] J. Frohlich. *Statistics of fields, the Yang-Baxter equation, and the theory of knots and links*. 1992.

[61] Gregory Moore and Nicholas Read. Nonabelions in the fractional quantum hall effect. *Nuclear Physics B*, 360(2):362–396, August 1991.

[62] X. G. Wen. Non-Abelian statistics in the fractional quantum Hall states. *Physical Review Letters*, 66(6):802–805, February 1991.

[63] J. K. Jain, S. A. Kivelson, and Nandini Trivedi. Scaling theory of the fractional quantum Hall effect. *Physical Review Letters*, 64(11):1297–1300, March 1990.

[64] R. H. Morf, N. d'Ambrumenil, and S. Das Sarma. Excitation gaps in fractional quantum Hall states: An exact diagonalization study. *Physical Review B*, 66(7):075408, August 2002.

[65] Csaba Toke and Jainendra K. Jain. Change in the character of quasiparticles without gap collapse in a model of fractional quantum Hall effect. *Physical Review B*, 80(20):205301, November 2009.

[66] Anne E. B. Nielsen, German Sierra, and J. Ignacio Cirac. Local models of fractional quantum Hall states in lattices and physical implementation. *Nature Communications*, 4(1):2864, November 2013.

[67] Dillip K. Nandy, N. S. Srivatsa, and Anne E. B. Nielsen. Truncation of lattice fractional quantum Hall Hamiltonians derived from conformal field theory. *Physical Review B*, 100(3):035123, July 2019.

[68] Emil J. Bergholtz and Zhao Liu. Topological flat band models and fractional chern insulators. *International Journal of Modern Physics B*, 27(24):1330017, September 2013.

[69] A. Sterdyniak, C. Repellin, B. Andrei Bernevig, and N. Regnault. Series of Abelian and non-Abelian states in $C > 1$ fractional Chern insulators. *Physical Review B*, 87(20):205137, May 2013.

[70] Michael Levin and Xiao-Gang Wen. Detecting Topological Order in a Ground State Wave Function. *Physical Review Letters*, 96(11):110405, March 2006.

[71] B. Estienne, N. Regnault, and B.A. Bernevig. Correlation Lengths and Topological Entanglement Entropies of Unitary and Nonunitary Fractional Quantum Hall Wave Functions. *Physical Review Letters*, 114(18):186801, May 2015.

[72] Ajit C. Balram, J. K. Jain, and Maissam Barkeshli. $\mathbb{Z}_n$ superconductivity of composite bosons and the 7/3 fractional quantum hall effect. *Physical Review Research*, 2(1):013349, March 2020.

[73] Ajit C. Balram and A. Wojs. Fractional Quantum Hall Effect at $\nu = 2+4/9$. *arXiv:2003.07038 [cond-mat]*, August 2020.

[74] Leon Schoonderwoerd, Frank Pollmann, and Gunnar Möller. Interaction-driven plateau transition between integer and fractional Chern Insulators. *arXiv:1908.00988 [cond-mat]*, August 2019. arXiv: 1908.00988.

[75] Bartholomew Andrews and Alexey Soluyanov. Fractional quantum Hall states for moiré superstructures in the Hofstadter regime. *Physical Review B*, 101(23):235312, June 2020.

[76] Moreover, this is far from the value taken by the closest non-Abelian competitor, the particle-hole conjugate of the four-cluster Read-Rezayi state, which has a topological entanglement entropy of $\gamma \approx 1.792$.

[77] The difficulty in computing higher filling fractions in the FQH hierarchy is not only due to the more restrictive geometry constraints but also due to the increased sensitivity of these states with respect to interaction strength and gap to width ratio.

[78] Michael P. Zaletel, Roger S. K. Mong, and Frank Pollmann. Topological Characterization of Fractional Quantum Hall Ground States from Microscopic Hamiltonians. *Physical Review Letters*, 110(23):236801, June 2013.

[79] Shiying Dong, Eduardo Fradkin, Robert G Leigh, and Sean Nowling. Topological entanglement entropy in Chern-Simons theories and quantum Hall fluids. *Journal of High Energy Physics*, 2008(05):016–016, May 2008.

[80] W. N. Faugno, J. K. Jain, and Ajit C. Balram. A non-Abelian fractional quantum Hall state at 3/7 filled Landau level. *Physical Review Research*, 2(3):033223, August 2020. arXiv: 2006.00238.

[81] Th. Jolicoeur. Non-Abelian States with Negative Flux: A New Series of Quantum Hall States. *Physical Review Letters*, 99(3):036805, July 2007.

[82] Ajit C. Balram, Maissam Barkeshli, and Mark S. Rudner. Parton construction of particle-hole-conjugate Read-Rezayi parafermion fractional quantum Hall states and beyond. *Physical Review B*, 99(24):241108, June 2019.

[83] Iván D. Rodríguez, Simon C. Davenport, Steven H. Simon, and J. K. Slingerland. Entanglement spectrum of composite fermion states in real space. *Physical Review B*, 88(15):155307, October 2013.

[84] Simon C. Davenport, Iván D. Rodríguez, J. K. Slingerland, and Steven H. Simon. Composite fermion model for entanglement spectrum of fractional quantum Hall states. *Physical Review B*, 92(11):115155, September 2015.

[85] N. Regnault, B. A. Bernevig, and F. D. M. Haldane. Topological Entanglement and Clustering of Jain Hierarchy States. *Physical Review Letters*, 103(1):016801, June 2009.

[86] The topological entanglement entropy is also negative, which is not physical.

[87] Jianyun Zhao, Yuhe Zhang, and J.K. Jain. Crystallization in the Fractional Quantum Hall Regime Induced by Landau-Level Mixing. *Physical Review Letters*, 121(11):116802, September 2018.

[88] B. Andrei Bernevig and F. D. M. Haldane. Properties of Non-Abelian Fractional Quantum Hall States at filling $\nu = k/r$. *Physical Review Letters*, 101(24):246806, December 2008.

[89] N. Read and E. Rezayi. Beyond paired quantum Hall states: Parafermions and incompressible states in the first excited Landau level. *Physical Review B*, 59(12):8084–8092, March 1999.

[90] N. Read. Non-Abelian adiabatic statistics and Hall viscosity in quantum Hall states and $p_x + ip_y$ paired superfluids. *Physical Review B*, 79(4):045308, January 2009.

[91] N. Goldman, J. C. Budich, and P. Zoller. Topological quantum matter with ultracold gases in optical lattices. *Nature Physics*, 12(7):639–645, July 2016.

[92] Eric M. Spanton, Alexander A. Zibrov, Haoxin Zhou, Takashi Taniguchi, Kenji Watanabe, Michael P. Zaletel, and Andrea F. Young. Observation of fractional Chern insulators in a van der Waals heterostructure. *Science*, 360(6384):62–66, April 2018.

[93] M. Hafezi, A. S. Sørensen, E. Demler, and M. D. Lukin. Fractional quantum Hall effect in optical lattices. *Physical Review A*, 76(2):023613, August 2007.

[94] Patrick J. Ledwith, Grigory Tarnopolsky, Eslam Khalaf, and Ashvin Vishwanath. Fractional Chern insulator states in twisted bilayer graphene: An analytical approach. *Physical Review Research*, 2(2):023237, May 2020.

[95] Cécile Repellin and T. Senthil. Chern bands of twisted bilayer graphene: Fractional Chern insulators and spin phase transition. *Physical Review Research*, 2(2):023238, May 2020.

[96] N.R. Cooper, J. Dalibard, and I.B. Spielman. Topological bands for ultracold atoms. *Reviews of Modern Physics*, 91(1):015005, March 2019.

[97] L. Tagliacozzo, Thiago. R. de Oliveira, S. Iblisdir, and J. I. Latorre. Scaling of entanglement support for matrix product states. *Physical Review B*, 78(2):024410, July 2008.

[98] Leon Schoonderwoerd. *Quantum Hall states in the Harper-Hofstadter model: existence, stability and novel phase transitions*. PhD thesis, University of Kent, 2020.

[99] Frank Pollmann, Subroto Mukerjee, Ari Turner, and Joel E. Moore. Theory of finite-entanglement scaling at one-dimensional quantum critical points. *Physical Review Letters*, 102(25):255701, June 2009. arXiv: 0812.2903.

[100] Pasquale Calabrese and John Cardy. Entanglement entropy and conformal field theory. *Journal of Physics A: Mathematical and Theoretical*, 42(50):504005, December 2009. arXiv: 0905.4013.

[101] Scott D. Geraedts, Michael P. Zaletel, Roger S. K. Mong, Max A. Metlitski, Ashvin Vishwanath, and Olexei I. Motrunich. The half-filled Landau level: The case for Dirac composite fermions. *Science*, 352(6282):197–201, April 2016.

[102] F. D. M. Haldane. Model for a Quantum Hall Effect without Landau Levels: Condensed-Matter Realization of the "Parity Anomaly". *Physical Review Letters*, 61(18):2015–2018, October 1988.

[103] D Jaksch and P Zoller. Creation of effective magnetic fields in optical lattices: the hofstadter butterfly for cold neutral atoms. *New Journal of Physics*, 5:56–56, may 2003.

[104] J.K. Slingerland and F.A. Bais. Quantum groups and non-abelian braiding in quantum hall systems. *Nuclear Physics B*, 612(3):229 – 290, 2001.

[105] Charlotte Gils, Simon Trebst, Alexei Kitaev, Andreas W. W. Ludwig, Matthias Troyer, and Zhenghan Wang. Topology-driven quantum phase transitions in time-reversal-invariant anyonic quantum liquids. *Nature Physics*, 5(11):834–839, Nov 2009.